

Searching for hadronic scale baryonic and dark forces at $(g - 2)_\mu$'s lattice-vs-dispersion front

Kaustubh Agashe ,^a **Abhishek Banerjee** ,^a **Minyuan Jiang** ,^b **Shmuel Nussinov** ,^b **Kushan Panchal** ,^a **Srijit Paul** ,^a **Gilad Perez** ,^d **Yotam Soreq** ,^e

^a*Maryland Center for Fundamental Physics, University of Maryland, College Park, MD 20742, USA*

^b*Deutsches Elektronen-Synchrotron DESY, Notkestr. 85, 22607 Hamburg, Germany*

^c*Tel Aviv University, 6195001, Tel Aviv, Israel*

^d*Department of Particle Physics and Astrophysics, Weizmann Institute of Science, Rehovot 761001, Israel*

^e*Physics Department, Technion - Israel Institute of Technology, Haifa 3200003, Israel*

ABSTRACT: The anomalous magnetic moment of the muon (a_μ) provides a stringent test of the quantum nature of the Standard Model (SM) and its extensions. To probe beyond the SM physics, one needs to be able to subtract the SM contributions, which consists of a non-perturbative part, namely, the hadronic vacuum polarization (HVP) of the photon. The state of the art is to predominantly use two different methods to extract this HVP: lattice computation, and dispersion relation-based, data-driven method. Thus one can construct different forms of the “ a_μ test” which compares the precise measurement of a_μ to its theory prediction. Additionally, this opens the possibility for another subtle test, where these two “theory” predictions themselves are compared against each other, which is denoted as the “HVP-test”. This test is particularly sensitive to hadronic scale new physics. Therefore, in this work, we consider an SM extension consisting of a generic, light $\sim (100 \text{ MeV} - 1 \text{ GeV})$ vector boson and study its impact on both tests. We develop a comprehensive formalism for this purpose. We find that in the case of data-driven HVP being used in the a_μ test, the new physics contributions effectively cancel for a flavor-universal vector boson. As an illustration of these general results, we consider two benchmark models: i) the dark photon (A') and ii) a gauge boson coupled to baryon-number (B). Using a combination of these tests, we are able to constrain the parameter space of B and A' , complementarily to the existing limits. As a spin-off, our preliminary analysis of the spectrum of the invariant mass of 3π in events with ISR at the B - factories (BaBar, Belle) manifests the value of such a study in searching for $B \rightarrow 3\pi$ decay, thus motivating a dedicated search by experimental collaborations.

Contents

1	Introduction	1
2	Generalities of the a_μ and HVP test	4
2.1	X contributions to the HVP and a_μ test	4
2.2	Explicit calculations	7
3	Existing constraints	9
4	New Physics Models	11
4.1	Dark Photon	11
4.2	Baryon Number Gauge Boson	13
5	Implications for and from lattice computation	18
5.1	Lattice scale setting error due to New Physics	18
5.2	Fine grained HVP test	19
6	Conclusions	21
A	Some field theoretic proofs	23
A.1	Longitudinal contributions to a_μ	23
A.2	2-loop calculations for a_μ and renormalization schemes	24
A.3	Renormalization scheme independence of a_μ	26
B	Further explorations of the tests and parameter space	29
B.1	Contour plots for the a_μ and HVP tests	29
B.2	Plots for different g_ℓ/g_q for the B boson	30
B.3	Plots of g_q vs. g_ℓ for B boson with a different m_B	33
B.4	Plots for various data-driven vs lattice HVP scenarios	33
C	Window quantities	39

1 Introduction

One of the most precise low energy tests of the Standard Model (SM) of particle physics is through the measurement of the muon's anomalous magnetic moment, $a_\mu \equiv (g - 2)_\mu/2$. The results of the Muon $g - 2$ collaboration at the Fermi National Accelerator Laboratory (FNAL) [1–3] are consistent with the Brookhaven National Laboratory (BNL) ones [4]. The combined world average is $a_\mu^{\text{exp}} = 116592059(22) \times 10^{-11}$ [2]. On the theory side, the

most uncertain part is related to the photon's hadronic vacuum polarization (HVP), which cannot be calculated in perturbation theory [5].

There are two competing methods to estimate the HVP. First, a data-driven (DD) method, obtained by using the measured $\sigma(e^+e^- \rightarrow \text{hadrons})$ along with dispersion relations, and second, by using lattice QCD. By using either of these methods, the corresponding SM theory predictions, $a_\mu^{\text{SM}} (= \text{DD or lat})$, can yield independent a_μ tests as

$$\Delta a_\mu^{\text{SM}} \equiv a_\mu^{\text{exp}} - a_\mu^{\text{SM}} (= \text{DD or lat}) . \quad (1.1)$$

Using the data from BaBar [6], SND [7, 8], and KLOE [9] experiments, the Muon $g - 2$ Theory Initiative (TI) 2020 [10] prediction of the leading HVP contribution is $(a_\mu^{\text{HVP}})^{\text{TI}} = 6931(40) \times 10^{-11}$. Plugging $(a_\mu^{\text{HVP}})^{\text{TI}}$ into the theory predictions for the SM, a_μ^{SM} , leads to $\sim 5\sigma$ deviation from a_μ^{exp} . More recently, based on the measurement of $\sigma(e^+e^- \rightarrow 2\pi)$, the CMD-3 collaboration presented an HVP value 3.7σ higher than that of the TI 2020 result [11, 12]. On the other hand, there have been several lattice calculations of the HVP contribution [13–19]. In this article, we focus on the BMW 2020 result¹, $(a_\mu^{\text{HVP}})^{\text{BMW}} = 7075(55) \times 10^{-11}$ [21]. Both CMD-3 and lattice predictions for a_μ are consistent with the experimental result.

Since the TI 2020 data-driven HVP is a measurement, it can be compared to the lattice prediction and define the HVP test [22]

$$\Delta a_\mu^{\text{HVP}} \equiv (a_\mu^{\text{HVP}})^{\text{DD}} - (a_\mu^{\text{HVP}})^{\text{lat}} . \quad (1.2)$$

The known HVP *puzzle* is when using DD=TI and the BMW for the lattice, which leads to $\Delta a_\mu^{\text{HVP}} \times 10^{11} = -144(68)$ i.e. a $\sim 2.1\sigma$ discrepancy. Ref. [23] has proposed several tests to shed light on the HVP puzzle in addition to what is discussed above. Among them are the comparison of the values of α and $\sin^2 \theta_W$ at different scales, and the comparison with data from muonium spectroscopy (see also [24]). We note that a combination of the BaBar [25], $\tau-$ decay [26], and CMD-3 [11] data, i.e., *exclusion* of the KLOE and SND, ameliorates the HVP tension, while a further combination of the BMW result with them, reduces the $(g - 2)_\mu$ anomaly to 2.8σ [26].

The HVP and the electro-weak precision tests are very sensitive to hadronic scale physics (however, it was shown in [27] that low energy extensions of the SM exist, in which the $(g - 2)_\mu$ sensitivity to the new fields is greatly ameliorated). Thus, it motivated the authors of [22, 28–30] to confront models consisting of a new gauge boson, X , of mass $m_X \lesssim \mathcal{O}(\text{GeV})$ having both leptonic and hadronic couplings with these tests. In this paper, we consider this class of models, assuming that the new gauge boson couples in a flavor-universal manner, and point out that there are two additional subtle, but important effects. First, if the X -hadronic couplings (g_q) are larger than the X -leptonic couplings (g_ℓ) by at least a loop factor, the X -photon mixing diagram can be as important as the 1-loop X contribution to a_μ , see Fig. 1b and Fig. 1a, respectively. Second, in case that the data-driven method is used to obtain the photon HVP for the a_μ test in Eq. (1.1),

¹There is also the latest 2024 result from BMW [20]. However, it has data-driven inputs in its computation. Hence, we choose the 2020 number as it is a purely lattice result.

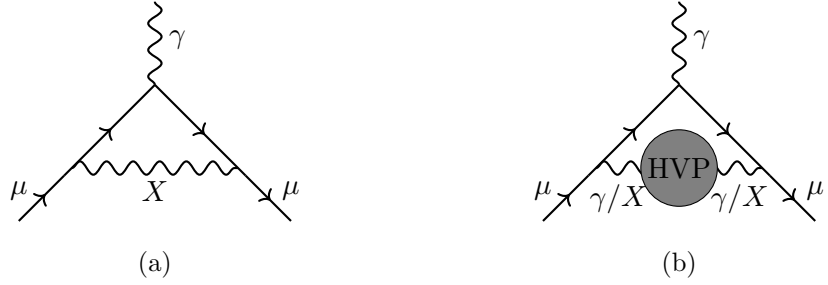


Figure 1: Relevant Feynman diagrams that contribute to the a_μ test. X is the new gauge boson. The diagrams are the $(g-2)_\mu$ contribution from 1-loop X (a), and through the vacuum polarization of photon and X (b).

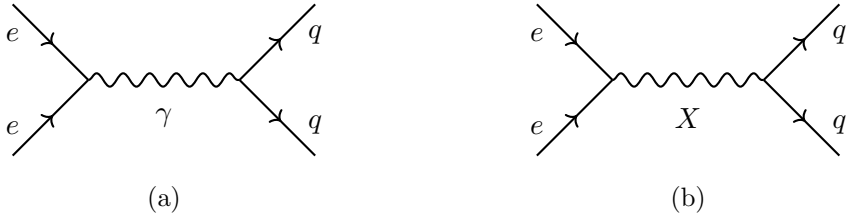


Figure 2: Relevant Feynman diagrams that contribute to $e^+e^- \rightarrow$ hadrons process, mediated by the photon (a) and X (b), and thus being relevant for the HVP test as well as the a_μ test when the data-driven method is used for the theoretical value of photon HVP.

the X on-shell contribution to the $e^+e^- \rightarrow$ hadrons cross section (Fig. 2b), which needs to be subtracted, cancels the 1-loop X contribution to $(g-2)_\mu$ from Fig. 1a, in the limit where the leptonic branching ratio of X is negligible. This effect results in a weaker sensitivity of a_μ to the 1-loop contribution of X , with the correction therein being a factor of $(1 - \mathcal{B}(X \rightarrow \text{had})) \sim g_\ell^2/g_q^2$.

To explore the phenomenological aspects of our observations, we consider two models of a new light gauge boson, namely a dark photon extension ($X = A'$) [31–36] and baryon number gauge boson one ($X = B$) [37–39]. These models offer complementary perspectives with different hierarchies of leptonic and hadronic charges, and isospin (I) representations. The dark photon has a lepton coupling similar to that of the quarks and has both $I = 1$ and $I = 0$ isospin components. Baryon number gauge boson on the other hand, couples predominantly to the quarks and has $I = 0$, with a small coupling to the leptons being generated through loop-induced kinetic mixing with the photon.

We supplement the above tests with a preliminary resonant search for the baryon number gauge boson in the 3π decay channel. We show that with on-tape BaBar and Belle data, see e.g. [25, 40], such a bump hunt in events with initial state radiation (ISR) can lead to potentially interesting results, and can possibly rule out the parameter space of the model.

The rest of the paper is organized as follows. In Section 2, we develop the formalism

for the a_μ and the HVP tests for a generic gauge boson X . We introduce the quantities relevant to those tests, outline the relevant computational methodologies, and discuss field theoretic insights alongside perturbative estimates in this section. In Section 3, we analyze existing constraints that are relevant to our study. In Section 4, we consider two benchmark new physics (NP) models: dark photon (Section 4.1) and baryon number gauge boson (Section 4.2) and show how they fare against both tests. We supplement Section 4.2 by providing a preliminary analysis of a bump hunt in the $\sigma(e^+e^- \rightarrow 3\pi)$ data. In Section 5.1, we discuss possible new physics effects in the lattice scale setting procedure, whereas in Section 5.2, we consider the window observables of the lattice simulations and consider the HVP test in various windows. We conclude in Section 6.

2 Generalities of the a_μ and HVP test

In this section, we develop the formalism for various quantities related to the HVP and the a_μ tests for a flavor-universal, but otherwise generic, gauge boson X . The SM fermions couple to the new gauge boson as $\mathcal{L} \supset g_X X_\mu J_X^\mu$ with $J_X^\mu = \sum_{\psi=\ell,u,d} Q_\psi^X \bar{\psi} \gamma^\mu \psi$ where ℓ , u , d denote charged leptons, up and down-type quarks, respectively. We define $g_\psi^X = g_X Q_\psi^X$. More explicitly, we define $g_q = g_u^X/Q_u^X = g_d^X/Q_d^X$ and $g_\ell = g_\ell^X$, and treat them as independent model parameters.

2.1 X contributions to the HVP and a_μ test

HVP test: This test involves reconciling the HVP contribution to a_μ from the data-driven approach and the lattice. In the data-driven approach, the HVP contribution to a_μ is obtained using the data of $e^+e^- \rightarrow$ hadron cross-section:

$$(a_\mu^{\text{HVP}})^{\text{DD}} = \frac{1}{4\pi^3} \int_{s_{\text{th}}}^\infty ds K(s) \sigma(e^+e^- \rightarrow \text{had}), \quad (2.1)$$

where $K(s)$ denotes the kernel function, and s_{th} is the integration threshold.

Including the new massive vector X , the total cross section is given by [22]

$$\sigma(e^+e^- \rightarrow \text{had}) = \int d\Pi |\mathcal{A}_{e^+e^- \rightarrow \gamma^* \rightarrow \text{had}} + \mathcal{A}_{e^+e^- \rightarrow X^* \rightarrow \text{had}}|^2 = \sigma^\gamma + \sigma^{\gamma-X} + \sigma^X, \quad (2.2)$$

see Fig. 2. Accordingly, the data-driven value of $(a_\mu^{\text{HVP}})^{\text{DD}}$ contains three contributions:

$$\begin{aligned} (a_\mu^{\text{HVP}})^{\text{DD}} &= \frac{1}{4\pi^3} \int_0^\infty ds K(s) (\sigma^\gamma + \sigma^{\gamma-X} + \sigma^X) \\ &\equiv (a_\mu^{\text{HVP}})_{e^+e^- \rightarrow \text{had}}^\gamma + (a_\mu^{\text{HVP}})_{e^+e^- \rightarrow \text{had}}^{\gamma-X} + (a_\mu^{\text{HVP}})_{e^+e^- \rightarrow \text{had}}^X. \end{aligned} \quad (2.3)$$

The lattice method for the HVP, on the other hand, is not contaminated by the presence of X , and can be identified the same as $(a_\mu^{\text{HVP}})_{e^+e^- \rightarrow \text{had}}^{\gamma-X}$. Therefore combining Eq. (1.2) and Eq. (2.3) lead to our master formula for the HVP test

$$\Delta a_\mu^{\text{HVP}} = (a_\mu^{\text{HVP}})_{e^+e^- \rightarrow \text{had}}^{\gamma-X} + (a_\mu^{\text{HVP}})_{e^+e^- \rightarrow \text{had}}^X. \quad (2.4)$$

a_μ test: This test involves reconciling the total a_μ from the experiment and SM through the relation in Eq. (1.1). By breaking it into the different new physics contributions (Fig. 1) we can write

$$\Delta a_\mu^{\text{SM}} = a_\mu^X + a_\mu^{\gamma-X} + a_\mu^{XX}. \quad (2.5)$$

The direct 1-loop X contribution to $(g-2)_\mu$ can be written as,

$$a_\mu^X = \int \frac{d^4 k}{(2\pi)^4} \frac{1}{k^2 - m_X^2} \times g_\ell^2 \mathcal{F}_\mu(k) \equiv \frac{g_\ell^2}{4\pi^2} K(m_X^2), \quad (2.6)$$

where $\mathcal{F}_\mu(k)$ encapsulates the rest propagators and vertices of the diagram, as well as a projection of the tensor structure into a_μ , and is common to all diagrams in Fig. 1. Note that, the kernel used here is the same as in Eq. (2.1). This is because by definition $K(s)$ denotes the direct 1-loop contribution to a_μ from a massive gauge boson of mass \sqrt{s} up to the coupling to the muons [5]. A direct evaluation of this kernel function gives [10, 34],

$$\begin{aligned} a_\mu^X &= \frac{g_\ell^2}{4\pi^2} K(m_X^2) = \frac{g_\ell^2}{4\pi^2} \int_0^1 dz \frac{z(1-z)^2}{(1-z)^2 + z m_X^2/m_\mu^2} \\ &= 196 \times 10^{-11} \left(\frac{g_\ell}{3 \times 10^{-3}} \right)^2 \left(\frac{0.6 \text{ GeV}}{m_X} \right)^2, \end{aligned} \quad (2.7)$$

where the last step holds for $m_X \gg m_\mu$.

As is well known in the literature, a direct X coupling to the muons reinstates the more than 5σ tension between the TI 2020 and the experimental result [10]. However, we notice that including only 1-loop contribution to ameliorate the $g-2$ anomaly may lead to the wrong conclusion, as the same coupling generates the 2-loop $\gamma-X$ mixing term $a_\mu^{\gamma-X}$ as well. To see the importance of this effect, let us consider the contribution to $a_\mu^{\gamma-X}$ from hadronic states in the blob, denoted as $(a_\mu^{\text{HVP}})^{\gamma-X}$. Assuming $Q_u^X \sim Q_d^X \sim \mathcal{O}(1)$, and including the color factor and the EM charges of the quarks, a perturbative estimates gives

$$\begin{aligned} (a_\mu^{\text{HVP}})^{\gamma-X} &\sim 2 \times 3 \times \left(\frac{2}{3} - \frac{1}{3} \right) \frac{e^2}{16\pi^2} \frac{g_\ell g_q}{16\pi^2} \frac{m_\mu^2}{m_X^2} \\ &\sim 10 \times 10^{-11} \left(\frac{g_\ell}{3 \times 10^{-3}} \right) \left(\frac{g_q}{0.15} \right) \left(\frac{0.6 \text{ GeV}}{m_X} \right)^2, \end{aligned} \quad (2.8)$$

for $m_X \gg m_\mu$. These rough estimates show that the mixing term could be as important as the 1-loop X contribution if $g_\ell/g_q \lesssim 10^{-3}$. Thus one expects that the 2-loop effects will be important if the gauge boson coupling to the hadrons is large compared to that of the leptons.

Considering the non-perturbative nature of the $\gamma-X$ mixing through hadronic states, to calculate $(a_\mu^{\text{HVP}})^{\gamma-X}$ properly, we use a dispersive method similar to the case of SM photon HVP calculation. Generally, the hadronic blob, defined as the momentum-space correlator of $J_{X,q}^\nu$ and the EM current J_{EM}^μ , can be written as $\Pi_{\gamma X}^{\mu\nu}(k^2) = (k^2 g^{\mu\nu} - k^\mu k^\nu) \Pi_{\gamma X}(k^2) + k^\mu k^\nu \Pi_{\gamma X}^L(k^2)$ with $\Pi_{\gamma X}^L(k^2)$ being the longitudinal part [41]. As shown in

Appendix A.1, the terms proportional to $k^\mu k^\nu$ do not contribute to $(g - 2)$, and thus we write

$$(a_\mu^{\text{HVP}})^{\gamma-X} = \int \frac{d^4 k}{(2\pi)^4} \frac{2e g_q \text{Re}(\bar{\Pi}_{\gamma X}(k^2))}{(k^2 - m_X^2)} \times e g_\ell \mathcal{F}_\mu(k), \quad (2.9)$$

where the bar on $\bar{\Pi}_{\gamma X}$ means it is renormalized. Like the case of photon HVP, we can use dispersion relation to obtain $\bar{\Pi}_{\gamma X}$ from its imaginary part $\text{Im}(\bar{\Pi}_{\gamma X})$, and recast $\text{Im}(\bar{\Pi}_{\gamma X})$ in terms of the interference contribution in the $e^+e^- \rightarrow \text{hadron}$ cross-section $\sigma^{\gamma-X}$. In the end, we obtain the simple relation:

$$(a_\mu^{\text{HVP}})^{\gamma-X}_{e^+e^- \rightarrow \text{had}} = (a_\mu^{\text{HVP}})^{\gamma-X} \approx a_\mu^{\gamma-X}, \quad (2.10)$$

where the last equality follows from the fact that $\gamma - X$ mixing through leptonic states is always much smaller than hadronic states at least by a factor of $(g_\ell/g_q)/4\pi$. We note that the above form of the equation is only valid when we renormalize $\Pi_{\gamma X}(k^2)$ at $k^2 = m_X^2$. The renormalization scheme independent physical observable is $a_\mu^{\gamma-X} + a_\mu^X$, a result we show in Appendix A.3.

Lastly, similar to $a_\mu^{\gamma-X}$, a perturbative estimate for a_μ^{XX} provides

$$a_\mu^{XX} \sim \frac{g_\ell^2}{16\pi^2} \frac{g_q^2}{16\pi^2} \frac{m_\mu^2}{m_X^2} \sim 0.02 \times 10^{-11} \left(\frac{g_\ell}{3 \times 10^{-3}} \right)^2 \left(\frac{0.6 \text{ GeV}}{m_X} \right)^2 \ll a_\mu^{\gamma-X}, \quad (2.11)$$

for $g_q = 0.15$. Thus a_μ^{XX} is parametrically much smaller than the other two contributions, and beyond the current precision of the measurement.

At this point, one might naively expect a relation $(a_\mu^{\text{HVP}})^X_{e^+e^- \rightarrow \text{had}} \sim a_\mu^{XX}$, similar to Eq. (2.10), and conclude that $(a_\mu^{\text{HVP}})^X_{e^+e^- \rightarrow \text{had}}$ is also negligible in the HVP test. However, this is not true. To see this, notice that under the narrow width approximation $\Gamma_X \ll m_X$, σ^X is dominated by on-shell X contribution: $\sigma^X \simeq \sigma(e^+e^- \rightarrow X) \mathcal{B}(X \rightarrow \text{had})$. This leads to:

$$\begin{aligned} (a_\mu^{\text{HVP}})^X_{e^+e^- \rightarrow \text{had}} &\simeq \mathcal{B}(X \rightarrow \text{had}) \frac{1}{4\pi^3} \int_{s_{\text{th}}}^\infty ds K(s) \sigma(e^+e^- \rightarrow X) \\ &= a_\mu^X \mathcal{B}(X \rightarrow \text{had}). \end{aligned} \quad (2.12)$$

With an estimation for both a_μ^X and $(a_\mu^{\text{HVP}})^{\gamma-X}$, and using Eq. (2.10) we have

$$\frac{(a_\mu^{\text{HVP}})^X_{e^+e^- \rightarrow \text{had}}}{a_\mu^{\gamma-X}} \sim \left(\frac{8\pi^2}{e^2} \times \frac{g_\ell}{g_q} \right) \mathcal{B}(X \rightarrow \text{had}) \sim 17 \left(\frac{g_\ell}{3 \times 10^{-3}} \right) \left(\frac{0.15}{g_q} \right) \mathcal{B}(X \rightarrow \text{had}). \quad (2.13)$$

Therefore, due to the on-shell enhancement, $(a_\mu^{\text{HVP}})^X_{e^+e^- \rightarrow \text{had}}$ can become larger than $a_\mu^{\gamma-X}$ and so, contributes significantly to the HVP test.

For the value of a_μ^{SM} in the a_μ test, one can use either lattice or data-driven results for the HVP part. For the first choice, we have using Eq. (1.1)

$$\Delta a_\mu^{\text{lat}} = a_\mu^X + a_\mu^{\gamma-X} + a_\mu^{XX} \simeq a_\mu^X + a_\mu^{\gamma-X}, \quad (2.14)$$

which we denote as the “lattice” a_μ test. In the last equality, we ignore the small a_μ^{XX} contribution. For the second choice, notice that a_μ^{DD} is not a pure SM contribution, see Eq. (2.4), we have

$$\begin{aligned}\Delta a_\mu^{\text{DD}} &= a_\mu^{\text{exp}} - a_\mu^{\text{DD}} = a_\mu^X - (a_\mu^{\text{HVP}})_{e^+e^- \rightarrow \text{had}}^X + a_\mu^{\gamma-X} - (a_\mu^{\text{HVP}})_{e^+e^- \rightarrow \text{had}}^{\gamma-X} + a_\mu^{XX} \\ &\approx a_\mu^X - (a_\mu^{\text{HVP}})_{e^+e^- \rightarrow \text{had}}^X + a_\mu^{XX}.\end{aligned}\quad (2.15)$$

where we obtain the last line using Eq. (2.10). This is denoted as the “data driven” a_μ test. In addition, under the narrow width approximation, we can use Eq. (2.12) and notice significant cancellation in the DD a_μ test, namely:

$$\Delta a_\mu^{\text{DD}} \simeq a_\mu^X [1 - \mathcal{B}(X \rightarrow \text{had})], \quad (2.16)$$

where we ignore the small a_μ^{XX} contribution. The above equation shows that a gauge boson which mostly decays to the hadrons i.e. $\mathcal{B}(X \rightarrow \text{had}) \sim 1$, is not sensitive to the data-driven a_μ test at all. Even for models such as the dark photon, this consideration is significant, as the branching ratio to hadrons is approximately $\mathcal{O}(80\% - 90\%)$ ($\sim \mathcal{O}(50\%)$) when the dark photon mass is near (away from) the hadronic resonances. We expect a similar effect for other observables which use data-driven method to estimate SM non perturbative contributions as in muonium spectroscopy, running of α and $\sin^2 \theta_W$ (see [23] for a related discussion).

2.2 Explicit calculations

As we showed above, the crucial input for both the HVP and the a_μ tests is the X contribution to the $\sigma(e^+e^- \rightarrow \text{hadrons})$ cross section, i.e. $\sigma^{\gamma-X}$ and σ^X . Here, we discuss how to determine them from data. This can be done by calculating the relative ratio between the $e^+e^- \rightarrow X^* \rightarrow Y$ and $e^+e^- \rightarrow \gamma^* \rightarrow Y$ amplitudes with Y an SM final state, which can be obtained by calculating the X mixing with the relevant vector meson, see [22, 36, 42] for this approach.

Depending on the Isospin of X , it can interfere with the ρ ($I = 1$) meson and contribute to 2π final state, and/or contribute to 3π , KK etc final states by interfering with the Iso-singlet ($I = 0$) vector mesons (ω, ϕ). For instance, for $Y = 2\pi$, the ratio is obtained by calculating the X mixing with the ρ meson current, $\rho^\mu \sim (\bar{u}\gamma^\mu u - \bar{d}\gamma^\mu d)$. It can be written as

$$\frac{\mathcal{A}_{e^+e^- \rightarrow X^* \rightarrow 2\pi}}{\mathcal{A}_{e^+e^- \rightarrow \gamma^* \rightarrow 2\pi}} = \frac{\epsilon_\rho s}{s - m_X^2 + im_X \Gamma_X}, \quad (2.17)$$

where, $\epsilon_\rho = g_\ell g_q (Q_u^X - Q_d^X)/e^2$. Thus the X contribution to $\sigma(e^+e^- \rightarrow 2\pi)$ can be obtained as,

$$\sigma_{2\pi}^{\gamma-X}(s) = \sigma_{2\pi}^{\text{SM}}(s) \times \frac{2\epsilon_\rho s(s - m_X^2)}{(s - m_X^2)^2 + m_X^2 \Gamma_X^2}, \quad \sigma_{2\pi}^X(s) = \sigma_{2\pi}^{\text{SM}}(s) \times \frac{\epsilon_\rho^2 s^2}{(s - m_X^2)^2 + m_X^2 \Gamma_X^2}, \quad (2.18)$$

where $\sigma_{2\pi}^{\text{SM}} = \sigma(e^+e^- \rightarrow \gamma^* \rightarrow 2\pi)$ denotes the cross-section through the SM photon, which can be safely approximated using the experimental data. $\sigma_{2\pi}^{\gamma-X}$ and $\sigma_{2\pi}^X$ denotes the SM- and X interference term and pure (on- and off- shell) X contribution respectively.

Similarly, the X contribution to $\sigma(e^+e^- \rightarrow 3\pi)$ can be obtained by looking at the mixing with ω meson ($\omega^\mu \sim \bar{u}\gamma^\mu u + \bar{d}\gamma^\mu d$), ϕ meson ($\phi^\mu \sim \bar{s}\gamma^\mu s$), and the $\omega - \phi$ contribution with the substitution of $\sigma_{2\pi}^{\text{SM}} \rightarrow \sigma_{3\pi}^{\text{SM}}$ in respective ω , ϕ and/or $\omega - \phi$ channels along-with $\epsilon_\rho \rightarrow \epsilon_\omega = 3g_\ell g_q (Q_u^X + Q_d^X)/e^2$, $\epsilon_\rho \rightarrow \epsilon_\phi = -3g_q g_\ell Q_d^X/e^2$, and $\epsilon_\rho \rightarrow \epsilon_{\omega\phi} = 3g_\ell g_q (Q_u^X + Q_d^X)/(2e^2)$ respectively, as discussed in [42]. For $m_X \gtrsim \text{GeV}$, it can also contribute to $e^+e^- \rightarrow K\bar{K}$ cross-section. The NP contribution to $\sigma(e^+e^- \rightarrow K\bar{K})$ can be obtained by looking at the mixing with ϕ meson with the substitution of $\epsilon_\rho \rightarrow \epsilon_\phi$ and $\sigma_{2\pi}^{\text{SM}} \rightarrow \sigma_{K\bar{K}}^{\text{SM},\phi}$. We obtain the SM contribution to $\sigma(e^+e^- \rightarrow \text{had})$ through the ratio

$$\mathcal{R}_\mu = \frac{\sigma(e^+e^- \rightarrow \text{had})}{\sigma(e^+e^- \rightarrow \mu^+\mu^-)} . \quad (2.19)$$

In computations of the HVP, we need to use the vacuum polarization (VP) subtracted cross-section, also known as the undressed cross section [5]. This is to avoid double counting between the leading and higher order HVP contributions. We use the tree-level value of $\sigma(e^+e^- \rightarrow \mu^+\mu^-)$ for the denominator of Eq. 2.19, which does not need undressing. We incur a small error (at higher order in QED) due to this approximation. However, since the NP contribution to $\sigma(e^+e^- \rightarrow \text{had})$ is itself a small correction to the SM contribution, the effect of the error from undressing, to the NP cross section, is doubly suppressed. One can obtain the decay width of X following the procedure outlined in [42]. The partial width of X to the leptons can be calculated perturbatively, while the hadronic for the hadronic width, we use the similar procedure of computing X contribution to $\sigma(e^+e^- \rightarrow \text{had})$ in various final states.

Next, we demonstrate the importance of the $\gamma - X$ mixing contribution to a_μ , which is relevant when $g_\ell \ll g_q$, beyond the above naive estimation. For simplicity, we assume that X has universal quark couplings, as in the case of $X = B$. We calculate $a_\mu^{\gamma-X}$ with the data-driven method and we plot the ratio of $a_\mu^{\gamma-X}/a_\mu^X$ in Fig. 3, for various values of the couplings (i.e. g_q and g_ℓ) and m_X .

Perturbative estimates show that these two term scale as $a_\mu^{\gamma-X}/a_\mu^X \sim (\alpha/2\pi)(g_q/g_\ell)$ which is comparable only for $g_\ell/g_q \sim 10^{-3}$. However, the hadronic blob enhances the $a_\mu^{\gamma-X}$ contribution in a non-trivial m_X dependent way. This behavior is depicted in Fig. 3a where we show contours of $a_\mu^{\gamma-X}/a_\mu^X$ as a function of g_ℓ/g_q and m_X . To understand the m_X dependence clearly, in Fig. 3b, we plot $(g_\ell/g_q)(a_\mu^{\gamma-X}/a_\mu^X)$ as a function of m_X . From the above plots, we see that the interference term increases as m_X approaches a hadronic resonance, only to decrease significantly once very close to it. This behavior can be understood in the following way. From Eq. (2.18) we see that the interference cross section depends on the product of $\sigma_{\text{had}}^{\text{SM}}(s)$ and $s(s - m_X^2)/((s - m_X^2)^2 + m_X^2 \Gamma_X^2)$. $\sigma_{\text{had}}^{\text{SM}}(s)$ increases as s approaches a hadronic resonance, and reaches a maximum for $\sqrt{s} = m_{\text{had}}$ where m_{had} is the mass of the resonance. On the other hand, $s(s - m_X^2)/((s - m_X^2)^2 + \Gamma_X^2 m_X^2)$ obtains maximum contribution for $\sqrt{s} = m_X \pm \Gamma_X$ rather than m_{had} . Thus the ratio of $a_\mu^{\gamma-X}/a_\mu^X$ increases as m_X nears a resonance, obtaining a maximum value around $m_X \pm \Gamma_X \simeq m_{\text{had}}$, and then drops sharply afterwards as m_X approaches m_{had} . Away from the resonances, $a_\mu^{\gamma-X}/a_\mu^X$ scales inversely with g_ℓ/g_q for a fixed m_X as expected from perturbative scaling.

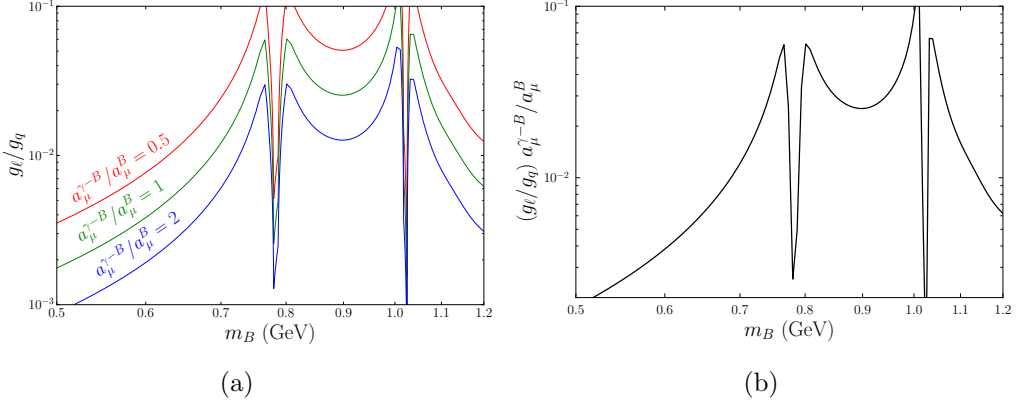


Figure 3: Plots of the ratio of the 1-loop and the $\gamma - X$ interference contribution to the $(g - 2)_\mu$. In Fig. (a), we show how does the ratio of the couplings g_ℓ/g_q changes as a function of m_X ($X = B$ boson) for fixed values of $a_\mu^{\gamma-X}/a_\mu^X$, whereas Fig. (b) depicts $a_\mu^{\gamma-X}/a_\mu^X$ as a function of m_X for fixed values of g_ℓ/g_q . A mild dependence on individual coupling enters through the decay width of X for m_X close to any hadronic resonances. We take $Q_u^X = Q_d^X$ and $g_q = 0.15$ to obtain these plots.

For $g_\ell/g_q \gtrsim 10^{-3}$, both the 1-loop and the mixing term would be small, despite their ratios being comparable. Hence, a considerable deviation from the “naive” a_μ test i.e. keeping only the 1-loop X contribution in $(g - 2)_\mu$ in Eq. (2.5), is only expected when $a_\mu^{\gamma-X}/a_\mu^X \sim \mathcal{O}(1)$ for larger couplings. We also note that there are higher loop contributions to the $(g - 2)$ such as the one shown in Fig. 4a denoted by $a_\mu^{\gamma-X-\gamma}$. The corresponding contribution in $\sigma(e^+e^- \rightarrow \text{had})$ would be the interference between the amplitudes given in Fig. 4b. Using Eq. (2.7) and Eq. (2.8), the typical size of these contributions can be estimated as $a_\mu^{\gamma-X-\gamma}/a_\mu^X = (a_\mu^{\gamma-X}/a_\mu^X)^2 \sim (\alpha/(2\pi) g_q/g_\ell \Pi)^2$, where Π captures the effects due to the hadronic blob. As shown in Appendix A.2, the one loop contribution to the renormalisation of g_ℓ , is also proportional to $(\alpha/2\pi)(g_q/g_\ell)\Pi$, which is required to be less than 1 to maintain perturbativity of g_ℓ . Ignoring the effect of the resonant enhancement which is only $\sim \mathcal{O}(10)$ when m_X is very close to hadronic resonances, the above requirement translates to a bound of $g_\ell/g_q \gtrsim 10^{-3}$. Therefore, these and higher loop order contributions to $(g - 2)$ and/or $\sigma(e^+e^- \rightarrow \text{had})$ can be safely neglected.

3 Existing constraints

In this section, we discuss the existing relevant constraints on X in addition to the $(g - 2)_\mu$.

($g - 2$) of electron: As X couples to electrons, it contributes to the anomalous magnetic moment of the electrons, $(g - 2)_e$ as well [34, 43]. By requiring the X induced contribution to be less than $\mathcal{O}(10^{-12})$, we obtain a bound on the lepton coupling as

$$g_\ell \lesssim 1 \times 10^{-2} \left(\frac{m_X}{0.6 \text{ GeV}} \right), \quad (3.1)$$

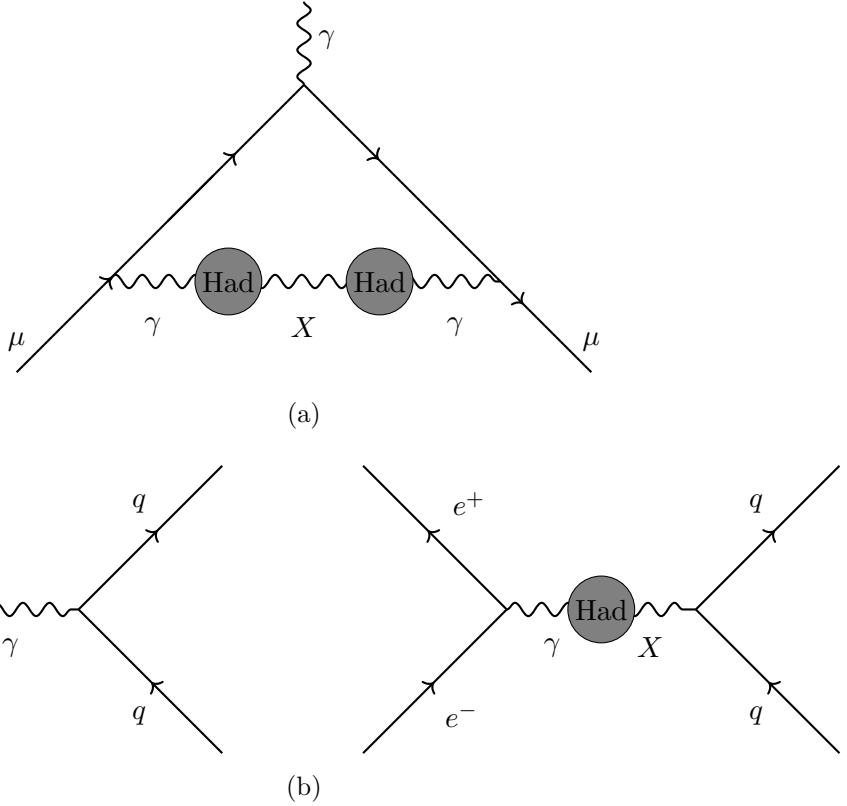


Figure 4: Correspondence between higher-loop ($g - 2$) contributions (above) and the higher loop $\sigma(e^+e^- \rightarrow \text{had})$ contributions (below).

where we use Eq. (2.7) with $m_\mu \rightarrow m_e$. Note that compared to a_μ , the HVP contribution to the theory prediction of $(g - 2)_e$ is small by a factor of $(m_e/m_\mu)^2$, and is well beyond the current measurement uncertainties [23].

Existing collider searches: X couples to the charged leptons, and decays visibly to the SM. Thus, the visible dark photon (A') searches from various experiments can be recast to our scenario. In the X mass range of our interest, $m_X \gtrsim 0.5$ GeV, the relevant constraints come from various $A' \rightarrow \mu^+\mu^-$ searches in BaBar [44], KLOE [45], CMS [46] and LHCb [47–49], Belle-II [50], and from $A' \rightarrow \pi^+\pi^-$ search in KLOE [9]. We use the [DarkCast](#) [42] framework to calculate the exclusion limits from the collider searches for the models we consider in the next section. Despite the exquisite sensitivity, due to large QCD background, the collider searches have blind spots close to the hadronic resonances (e.g. [48]), leading to unconstrained parameter space.

Rare Meson decay: Various rare meson decays may constrain the X coupling to the SM quarks. These constraints are of relevance if $g_q \gg g_\ell$ which is the case for baryon number gauge boson i.e. $X = B$. In particular, in the presence of an X coupling to the bottom quark, through the s channel exchange, $\Upsilon(1S)$ can decay to hadrons. The ratio of the branching fractions $\Delta R_\Upsilon = \Gamma(\Upsilon \rightarrow Z'^*, \gamma^* \rightarrow jj)/\Gamma(\Upsilon \rightarrow \mu^+\mu^-)$ can be used to

constrain g_q [37, 38]. From the limit on the non-EM dijet decay of $\Upsilon(1S)$, $\Delta R\Upsilon \lesssim 2.48$ at 95% C.L. [51] excludes a coupling of

$$g_q \lesssim 0.15, \quad (3.2)$$

in the mass range of $m_X \lesssim m_\Upsilon \sim 10$ GeV. Similarly, a rare decay of $\eta \rightarrow \pi^0\gamma\gamma$, and/or $\eta' \rightarrow \pi^+\pi^-\pi^0\gamma$ can be used to constrain g_q as well. For some specific m_X , these processes yield stringent constraints on g_q than that of the Υ decay, see [39] for a detailed discussion for the case of $X = B$.

LEP-II bound: The cross section of $e^+e^- \rightarrow q\bar{q}$ is measured with 1% accuracy by the LEP and/or LEP-II collaboration [52] with an appropriate theoretical prediction [53]. In the presence of X , (mostly) due to the $\gamma - X$ and $Z - X$ interference, the $e^+e^- \rightarrow q\bar{q}$ cross-section receives an additional contribution. By requiring the NP contribution is within the accuracy of the measurement, we obtain a bound on the product of the couplings as,

$$|g_\ell \times g_q(11.3Q_u^X - 8.9Q_d^X)| \lesssim 10^{-2}. \quad (3.3)$$

As the center of mass energy of LEP is much higher than m_X , this bound is independent of m_X . Note that, for most of the parameter space, the LEP bound is weaker than the already discussed constraints.

Mass difference of pions: For generic Q_u^X and Q_d^X , X breaks Isospin, and thus contribute to the Isospin breaking observables such as the mass splitting of the charged and neutral pions. Analogous to the case of SM photon, X contribution to pion mass difference is proportional to $g_q(Q_u^X - Q_d^X)$. Thus by rescaling the SM prediction from lattice QCD, and comparing it with the experimentally measured mass splitting at 95% C.L., one obtains a bound of [22, 54]

$$|g_q(Q_u^X - Q_d^X)| \lesssim 6 \times 10^{-2}. \quad (3.4)$$

4 New Physics Models

In this section, we apply the a_μ and HVP tests to phenomenologically interesting models. We consider (i) the dark photon (A') [32, 34, 55] and (ii) the baryon number gauge boson (B) [37–39]. In all the exclusion plots, the bounds from our proposed HVP and a_μ tests are depicted by the dark red and green lines respectively, whereas all the relevant existing bounds (discussed in Sec. 3) are shown by gray lines and shaded regions. The naive a_μ test i.e. 1-loop contribution to a_μ is depicted by blue dashed lines.

4.1 Dark Photon

We consider the dark photon interaction with the SM as $\mathcal{L} \supset e\varepsilon J_{\text{EM}}^\mu A'_\mu$ with ε being the kinetic mixing (KM) parameter. Thus, from the generic case of X boson, we obtain the dark photon phenomenology by substituting $Q_u^X = 2/3$, $Q_d^X = -1/3$, $Q_l^X = 1$ and $g_\ell = g_q = e\varepsilon$. The dark photon morphs the properties of the SM photon, and like the SM photon it

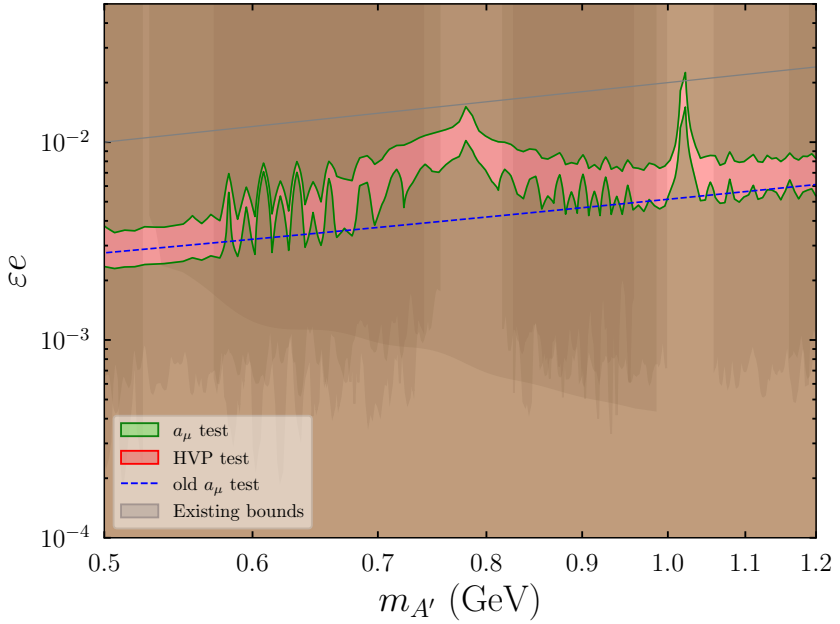


Figure 5: Parameter space of the dark photon coupling εe as a function of its mass $m_{A'}$ for the data driven a_μ test (c.f. Eq. (2.16)). We use TI 2020 as the DD value for both the a_μ and HVP tests. The red and green shaded regions are excluded by the $\pm 2\sigma$ HVP and a_μ tests, respectively, whereas the gray lines depict the existing bounds (see Section 3 for details). The brown colour in the plot is due to the overlap of the green and red shades. Therefore, brown regions are excluded by both the HVP and a_μ tests. The blue dashed line shows the contribution from $a_\mu^{A'}$ (naive a_μ test).

contributes to all the hadronic final states in the $\sigma(e^+e^- \rightarrow \text{had})$. Next, we discuss the result of subjecting the dark photon to the a_μ and HVP tests. In Fig. 5 and 6, we show the constraints from the HVP and a_μ test in dark red and green respectively, on the parameter space of εe and $m_{A'}$. In Fig. 5, we consider the data driven a_μ test (c.f. Eq. (2.16)). We use TI 2020 as the DD value for both the a_μ and HVP tests. Using them, we exclude hitherto uncharted territory of the dark photon parameter space; even for arbitrarily small coupling. This can be understood as follows: to satisfy the HVP test, we need (c.f. Eq. 2.4, 2.10, 2.12) $\Delta a_\mu^{\text{HVP}} \approx a_\mu^{\gamma-A'} + a_\mu^{A'} \mathcal{B}(A' \rightarrow \text{had}) = (-144 \pm 68) \times 10^{-11}$. Since $a_\mu^{A'}$ is always positive, and the interference is small, the HVP test is never satisfied. On the other hand, to satisfy the DD a_μ test, a large positive contribution from $a_\mu^{A'}$ is required to resolve the 5σ tension as (c.f. Eq. (2.16)) $\Delta a_\mu^{\text{DD}} = a_\mu^{A'} [1 - \mathcal{B}(A' \rightarrow \text{had})] = (249 \pm 48) \times 10^{-11}$ where we use the DD a_μ value from [10]. Since $\mathcal{B}(A' \rightarrow \text{had}) \sim 1 (\sim 1/2)$ when $m_{A'}$ is near (away) a hadronic resonance, the cancellation in Eq. (2.16) is significant, and thus making it virtually impossible to satisfy the a_μ test as well.

In Fig. 6, we consider the lattice version of the a_μ test (c.f. Eq. (2.14)) as $\Delta a_\mu^{\text{lat}} \approx a_\mu^{\gamma-A'} + a_\mu^{A'} = (105 \pm 61) \times 10^{-11}$ where we take the BMW 2020 result as lattice value [21]. We find that a_μ test improves the bound on the dark photon parameter space by $\mathcal{O}(10)$ for

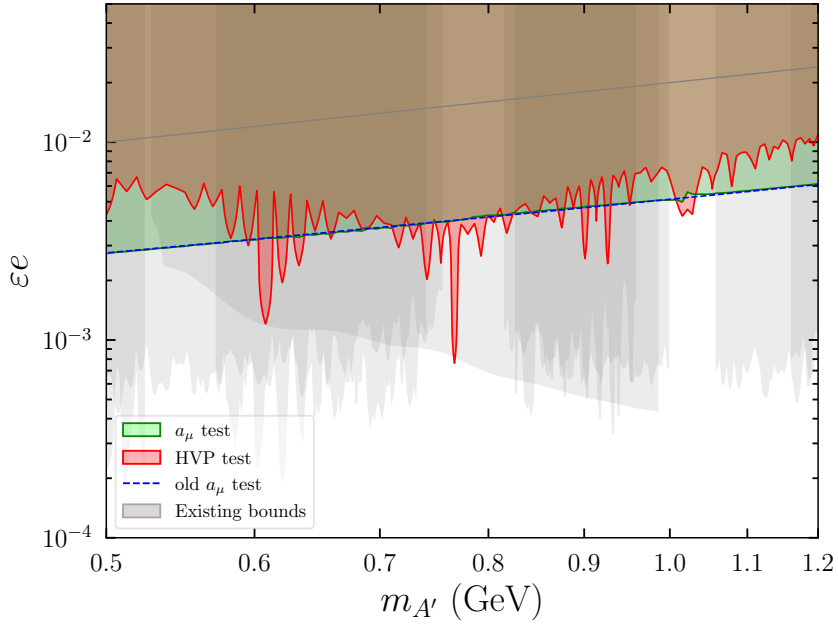


Figure 6: Parameter space of the dark photon coupling εe as a function of its mass $m_{A'}$ for the lattice a_μ test (c.f. Eq. (2.14)). We use BMW result for the a_μ test [20]. For the HVP test, we take a conservative approach. We consider a possibility that in the future, the central values of the data driven HVP and the lattice result match i.e. $(a_\mu^{\text{HVP}})^{\text{DD}} = (a_\mu^{\text{HVP}})^{\text{lat}}$. The rest of the figure matches the description of Fig. 5

$m_{A'}$ close to the ϕ resonance, where the collider searches have blind spots. The blue dashed line depicts the bound from direct 1-loop contribution $a_\mu^{A'}$, which is almost identical to the full a_μ test. This is expected because as $g_q = g_\ell = e\varepsilon \ll 1$, the mixing term $a_\mu^{\gamma-A'}$ is small compared to the 1-loop contribution even with the hadronic enhancement factor. For the HVP test, we take a conservative approach. We consider a possibility that in future the central values of the data driven HVP and the lattice result match with their respective error bars i.e. $(a_\mu^{\text{HVP}})^{\text{DD}} = (a_\mu^{\text{HVP}})^{\text{lat}}$. We take error bars to be the current combined value of 68×10^{-11} . We notice that the exclusion from the HVP test overlaps significantly with that of the a_μ test. We finish the section by noting that, if one considers the possibility of matching the DD HVP to the lattice result within $\pm 1\sigma$ of the current error combined bar i.e. $(a_\mu^{\text{HVP}})^{\text{DD}} = (a_\mu^{\text{HVP}})^{\text{lat}} \pm 1\sigma$, the bound from the HVP test improves upon the a_μ test by a factor of $\mathcal{O}(3-4)$. We defer this discussion to Appendix B.4.

4.2 Baryon Number Gauge Boson

Next, we discuss the second model – gauging the global baryon number $U(1)_B$ i.e. $X = B$. At the tree level B couples to the quarks, whereas a small coupling to the leptons is generated through the kinetic mixing with the hypercharge gauge boson. Thus, unlike the case of dark photon, the $\gamma - B$ mixing contribution would be relevant for both the a_μ and the HVP test. Below the weak scale, we consider the following low-energy Lagrangian

as [39]

$$\mathcal{L} \supset -\frac{\varepsilon_B}{2} B_{\mu\nu} F^{\mu\nu} + g_q B_\mu \bar{q} \gamma^\mu q \longrightarrow B_\mu [(g_q + Q_q^{\text{EM}} g_\ell) \bar{q} \gamma^\mu q - g_\ell \bar{\ell} \gamma^\mu \ell] , \quad (4.1)$$

where, q denotes the quarks with g_q being the flavor universal coupling of B , ε_B is the kinetic mixing between B and photon and the arrow denotes a basis transformation of $A \rightarrow A + \varepsilon_B B$ and $B \rightarrow B$ where the gauge kinetic terms are diagonalized. Upon diagonalizing, we obtain the B coupling to the SM quarks and charged leptons as $g_{u,d} = g_q + Q_{u,d}^{\text{EM}} g_\ell \simeq g_q$, and g_ℓ , respectively. Note that there is a minus sign in front of g_ℓ in the Lagrangian above because $Q_\ell^{\text{EM}} = -1$.

To estimate the size of g_ℓ , one can consider a UV completion such that either $U(1)_Y$ and/or $U(1)_B$ is embedded in a non-abelian gauge group at some scale Λ making $\varepsilon_B(\Lambda) = 0$. In such cases, the natural size of the lepton coupling can be estimated to be $g_\ell \gtrsim \alpha g_q / (4\pi)[c_1 \log(\Lambda/v_{\text{EW}}) + c_2 \log(v_{\text{EW}}/m_B)]$ where c_i 's depend on the specific UV model [38]. In our case, we are interested in large couplings, and thus, we do not resort to any particular UV completion. Thus, hierarchical coupling strengths between various SM sectors are obtained naturally in the case of $U(1)_B$ [37]. We note that, in the basis where B couplings to the quarks are flavor universal, there is no lepton coupling to B but $\varepsilon_B \neq 0$. On the other hand, a flavor non universal quark coupling elucidates non zero g_ℓ . Thus, only the sum of ε_B and g_ℓ represents a basis independent physical quantity, similar to the case of choosing oblique/non-oblique basis as discussed in [56]. In the first case, free theory parameters are g_q and ε_B , whereas in the second case, they are g_q and g_ℓ .

Another remark is in order. There are triangle anomalies involving the mixed $U(1)_B$ and SM gauge currents [57]. These necessitate the need of adding new physics (anomalons) to cancel the anomalies. Introducing anomalons leads to generation of Wess-Zumino terms involving B with SM W and Z bosons, and may result in a much stronger bound on g_q than the previously considered ones for $m_B \sim \mathcal{O}(\text{GeV})$ [58, 59]. However, these can be evaded by UV model building as discussed in [60–63]. We obtain the B contribution to $\sigma(e^+e^- \rightarrow \text{had})$ by following the discussion around Eq. (2.17) and (2.18) and using $Q_{u,d}^X = 1$. As already discussed, $U(1)_B$ is mostly Isospin singlet, with a small Isospin breaking contribution coming from the mixing with the SM photon. Thus it contributes mostly to the Iso-singlet final states such as 3π , $K\bar{K}$ etc. As can be seen from Eq. (2.17), B contribution to the 2π final states is proportional to $\epsilon_\rho \propto g_\ell^2 \ll \epsilon_{\omega,\phi}$.

In Fig. 7, we perform the data-driven a_μ test (c.f. Eq. (2.15)). Both for the HVP test (c.f. Eq. (2.4)) and the a_μ tests, we take TI 2020 as the data driven value. Using them, we exclude hitherto uncharted territory of the B boson parameter space shown by the dark red and green shaded region respectively; even for arbitrarily small couplings. To understand this, note that NP is necessary to satisfy either of the tests at the $\pm 2\sigma$ level. To satisfy the HVP test, we need (c.f. Eq. 2.4, 2.10, 2.12) $\Delta a_\mu^{\text{HVP}} \approx a_\mu^{\gamma-B} + a_\mu^B \mathcal{B}(B \rightarrow \text{had}) = (-144 \pm 68) \times 10^{-11}$. Since $\mathcal{B}(B \rightarrow \text{had}) \sim 1$ for $m_B \gtrsim 0.6 \text{ GeV}$ and a_μ^B is always positive, satisfying the HVP test requires large negative $a_\mu^{\gamma-B}$. As shown in Fig. 3, the mixing term is only relevant for $g_q/g_\ell \gg 1$ with sizable g_ℓ . Thus, a large negative mixing with not so large g_ℓ can be obtained close to the hadronic resonances, and we see two small

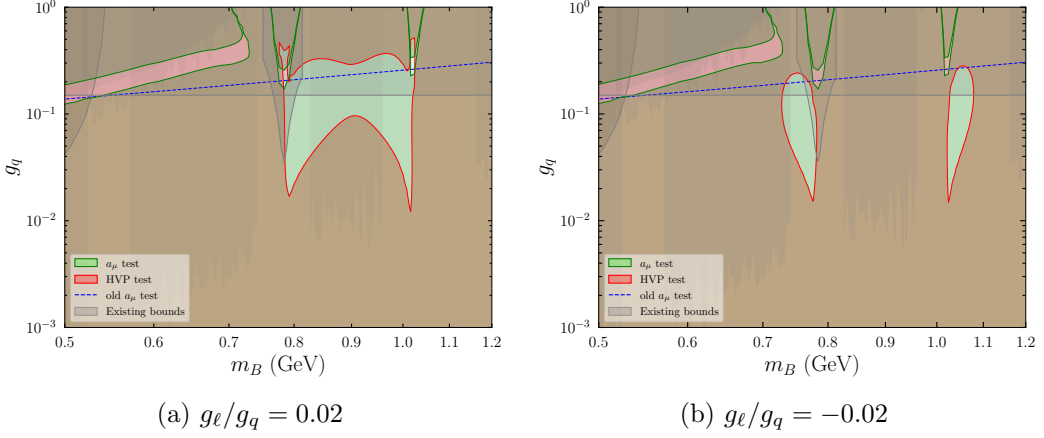


Figure 7: Parameter space of the quark coupling g_q as the function of the mass of B mass (m_B) for $g_\ell/g_q = 0.02$ (Fig. 7a) and $g_\ell/g_q = -0.02$ (Fig. 7b). In this plot, we consider the data-driven a_μ test (c.f. Eq. (2.15)). Both for the HVP test (c.f. Eq. (2.4)) and the a_μ , we take TI 2020 as the data driven value. The green and red regions show the $\pm 2\sigma$ exclusion by the a_μ and HVP tests respectively. The blue dashed line shows 1-loop B contribution a_μ^B (c.f. Eq. (2.6)), whereas the gray bands depict the existing constraints (see Sec. 3 for details).

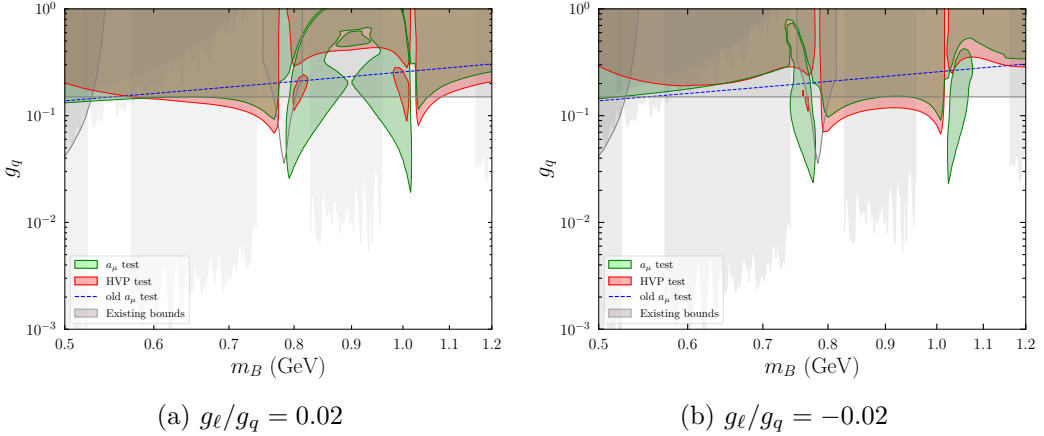


Figure 8: Parameter space of the quark coupling g_q as the function of the mass of B mass (m_B) for $g_\ell/g_q = 0.02$ (Fig. 8a) and $g_\ell/g_q = -0.02$ (Fig. 8b). In these plots, we perform the lattice a_μ test (c.f. Eq. (2.14)) by taking the BMW result as the SM contribution. For the HVP test (c.f. Eq. (2.4)), we consider a futuristic conservative possibility of the central values of the data driven HVP and the lattice result to match with each other within their respective error bars. The rest of the figure matches the description of Fig. 7

closed shaped regions where the HVP test is satisfied. In the rest of the parameter space, we rule out arbitrary small couplings using the HVP test. At the same time, satisfying DD a_μ test requires (c.f. Eq. (2.16)) $\Delta a_\mu = a_\mu^B [1 - \mathcal{B}(B \rightarrow \text{had})] = (249 \pm 48) \times 10^{-11}$. As $\mathcal{B}(B \rightarrow \text{had}) \sim 1$ for large m_B and the cancellation is exact in the narrow width

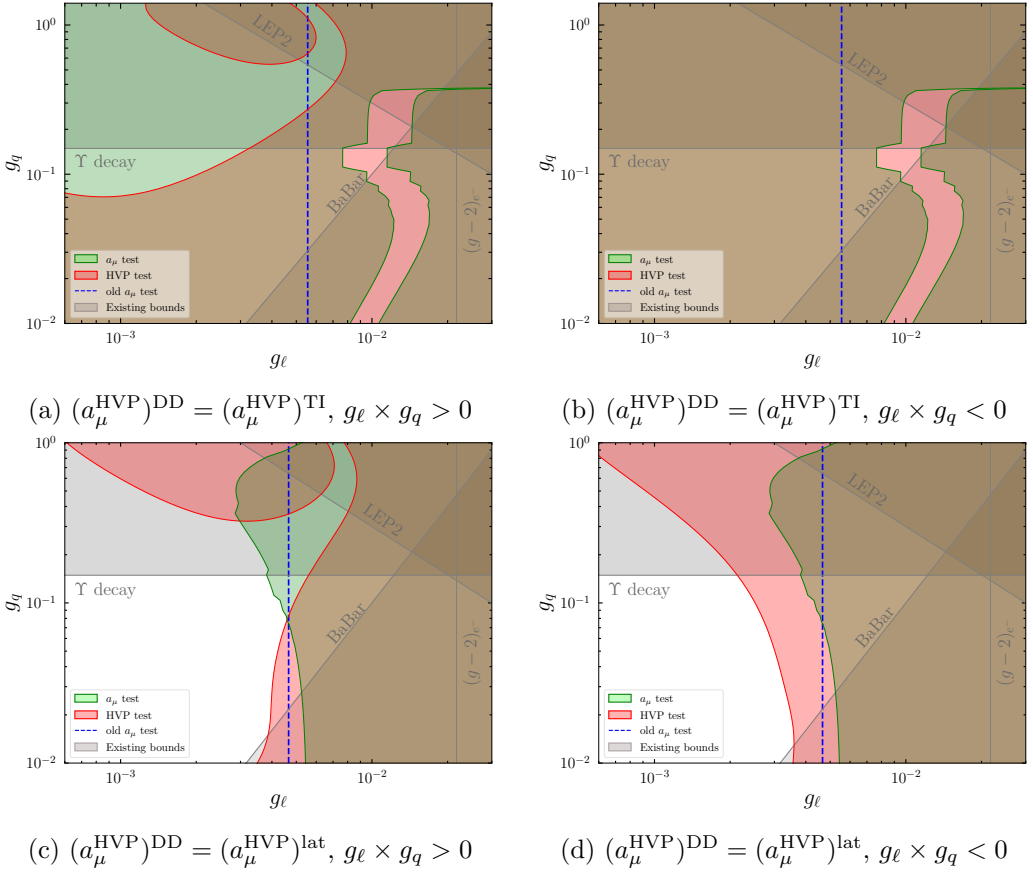


Figure 9: Plot of g_q vs g_ℓ for a fixed of $m_B = 0.9$ GeV both for positive and negative ratio. For the plots with $g_\ell \times g_q < 0$, we always consider $g_q > 0$ and plot $|g_\ell|$. In Fig. 9a and 9b, we perform the data-driven a_μ test (c.f. (2.15)) and take the TI 2020 value for the HVP test, whereas in Fig. 9c and 9d, we consider the lattice a_μ test (c.f. (2.5)) and take the data-driven HVP to be equal to the lattice result for the HVP test. The gray lines depict various existing constraints (see Sec. 3 for details). The colour scheme is the same as Fig. 7.

approximation, a significant deviation from this is necessary to satisfy the DD a_μ test. This can be obtained either in the small mass limit, or for large g_ℓ and g_q , or both. This observation can be validated by the observation that the region of the parameter space that is not shaded in green, requires large and thus previously excluded g_q . Both the tests exclude arbitrarily small couplings irrespective of the sign of the interference term as can be seen by the overlapping green and red regions in Fig. 7a and Fig. 7b. Exclusion plots for various other values of g_ℓ/g_q (positive and negative) can be found in Appendix B.2.

In Fig. 8, we consider the lattice a_μ test (c.f. Eq. (2.14)). Unlike the case of dark photon, we see a considerable deviation from the naive a_μ test for $m_B \gtrsim 0.6$ GeV. This is because the mixing term becomes important for B boson as $g_q \gg g_\ell$ as shown in Fig. 3. As before (c.f. Fig. 6), we consider the futuristic conservative possibility for the HVP

test: $(a_\mu^{\text{HVP}})^{\text{DD}} = (a_\mu^{\text{HVP}})^{\text{lat}}$. Using both the tests, we improve the sensitivity on the B parameter space by a factor of 4 where the existing collider searches have limited to zero sensitivities. As before red and green shaded regions depict the exclusion limits from the HVP and the a_μ test respectively. To understand the exclusion limits, notice that to satisfy the HVP test with $(a_\mu^{\text{HVP}})^{\text{DD}} = (a_\mu^{\text{HVP}})^{\text{lat}}$ and the lattice a_μ test within the $\pm 2\sigma$ value, no new physics is required, making $g_\ell, g_q \rightarrow 0$ consistent unlike the case discussed in Fig. 7. However, a positive $a_\mu^{\gamma-B}$ along with a positive a_μ^B , can provide a NP contribution above $+2\sigma$ value, and excludes the parameter space. On the other hand, a large mixing term, can provide a significant negative contribution and exclude the parameter space at -2σ value as well. This happens for $m_B \sim m_{\text{had}}$ and depends on the sign of g_ℓ/g_q as can be seen from both Fig. 8a and Fig. 8b.

From the above plots, we see the complementarity of the HVP test and the a_μ test i.e. there are regions of parameter space that satisfy either of the tests but excluded by the other one. To gain more insight, in Fig. 9, we plot g_q as a function of g_ℓ for a fixed mass. As an example we set $m_B = 0.9 \text{ GeV}$. We show similar plots for a different m_B in Appendix B.3. Similar to Fig. 7, in Fig. 9a and 9b, we consider the DD a_μ test for positive and negative g_ℓ/g_q respectively with TI 2020 values. We see that the a_μ test is satisfied only in a small region where g_ℓ/g_q is large, effectively making the cancellation in Eq. (2.16) inexact. At the same time, a large g_ℓ increases the a_μ^X contribution (c.f. Eq. (2.6)), leading to fulfillment of the test. However, as $m_B \gtrsim m_\phi$ and $\epsilon_\phi < 0$ for positive couplings, $\sigma^{\gamma-B}$ (c.f. Eq. (2.18)) and thus, $a_\mu^{\gamma-B}$ are positive, and HVP test is never satisfied in this case. Despite $g_\ell \times g_q < 0$, we see similar behaviour in Fig. 9b as well. Similar to Fig. 8, in Fig. 9c and 9d, we consider the lattice a_μ test to show the parameter space of g_ℓ vs g_q for $m_B = 0.9 \text{ GeV}$. We see that, for regions not already excluded by existing constraints, the HVP test fares slightly better than the a_μ test in this case, improving the bound on both g_ℓ and g_q by more than a factor of 4. Again, as expected, the interference term is relevant when $g_q \gtrsim g_\ell$, and for small g_q , both the tests approach the bound from the 1-loop contribution. This behavior can be seen in the plots by converging red, green and blue dashed lines. We finish the section by noting that, if one considers the possibility of matching the DD HVP to the lattice result within $\pm 1\sigma$ of the current combined error bar i.e. $(a_\mu^{\text{HVP}})^{\text{DD}} = (a_\mu^{\text{HVP}})^{\text{lat}} \pm 1\sigma$, the complementarity of the HVP test and the a_μ test becomes much more manifested and the bounds improve by a factor of $\mathcal{O}(2-4)$. We defer this discussion to Appendix B.4.

Resonant B search: We end this section by estimating the reach of a bump hunting in the $I = 0$ hadronic spectrum [25, 40, 64]. Among other channels [64, 65], a bump hunt in $\sigma(e^+e^- \rightarrow 3\pi)$ channel can be used to find/rule out the B boson.

To perform a preliminary analysis, we consider a bump hunt with Gaussian signal shape and data driven background estimation. We obtain the upper-limit (ul) of NP cross section as $\sigma_{\text{NP}}^{\text{ul}} \lesssim 2\sqrt{N_{\text{eve}}} / (\mathcal{L}_{\text{eff}} \times \epsilon_{\text{eff}} \times R)$, where N_{eve} of a given bin is obtained by summing the number of events in 4 neighboring bins, \mathcal{L}_{eff} is obtained by multiplying ISR differential luminosity with the effective energy resolution. ϵ_{eff} and R are the detection efficiency as a function of mass, and a radiative correction that accounts for the distortion of the

mass spectrum due to emission of several photons respectively. The choice of only taking the 4 neighboring bins is well suited for a narrow resonance, where the signal contribution diminishes rapidly outside the central bin, provided that the bin width exceeds the intrinsic width of the resonance [47]. In contrast, for broader resonances or in cases where the new physics signal extends beyond a single bin, a statistically significant excess of events would be observable across multiple adjacent bins relative to the expected background.

First, we consider the BaBar $e^+e^- \rightarrow 3\pi + \gamma$ measurement [25]. In this case, there are correlated errors for $\sqrt{s} \lesssim 1.1$ GeV. However, to simplify our analysis, we ignore this effect. We consider 3 sample resonance points as m_B : a) 0.75 GeV, b) 0.9 GeV, and c) 1.1 GeV. By using, $\mathcal{L}_{\text{int}} = 469 \text{ fb}^{-1}$ and $R = 1.0077$ as given and taking mass independent detection efficiency to be $\epsilon_{\text{eff}} \simeq 11\%$, we obtain an upper limit on $g_{\ell}^{\text{ul}} \times \sqrt{\mathcal{B}(B \rightarrow 3\pi)} \lesssim \{3 \times 10^{-4}, 2 \times 10^{-4}, 2 \times 10^{-4}\}$ for the above data points respectively. Next, we do a similar analysis using Belle-II $e^+e^- \rightarrow 3\pi + \gamma$ measurement [40]. We use $\mathcal{L}_{\text{int}} = 191 \text{ fb}^{-1}$, $R = 1.0080$ and $\epsilon_{\text{eff}} \simeq 10\%$, we obtain an upper limit on $g_{\ell}^{\text{ul}} \times \sqrt{\mathcal{B}(B \rightarrow 3\pi)} \lesssim \{3 \times 10^{-4}, 2 \times 10^{-4}, 10^{-3}\}$ for the same sample points respectively. With an improved luminosity of $\mathcal{L}_{\text{int}} = 50 \text{ ab}^{-1}$, the reach of Belle-II would be improved by a factor of 4. In addition to the bump hunt in the 3π channel, another way to look for B is in the decays of Charmonium and/or Bottomonium. In particular, we can look for final states where the photon is replaced by B in the radiative decays of such states. A similar analysis for $\phi \rightarrow \eta B, B \rightarrow \pi^0 \gamma$ has been performed by KLOE [39, 65]. However, this is only relevant for $0.3 \text{ GeV} \lesssim m_B \lesssim 0.5 \text{ GeV}$, as $\mathcal{B}(B \rightarrow \pi^0 \gamma)$ becomes negligible otherwise.

5 Implications for and from lattice computation

In this section we discuss the implication of the new physics models on the scale setting on the lattice [66]. In particular, we estimate the NP contribution to the most commonly used Ω^- baryon physical scale, which may impact all lattice predictions. Next, we emphasize the impact of new physics on the window quantities proposed in Ref. [67] by re-evaluating the bounds from the HVP test.

5.1 Lattice scale setting error due to New Physics

Lattice QCD predictions of physical quantities are intrinsically dependent on a energy scale \mathcal{S} , which is set by matching an independently computed precise lattice observable O_{lat} to its corresponding experimental value O_{exp} . The predictions are sensitive to the choice of this observable and the uncertainty associated with it. The experimental value of O_{exp} always includes electromagnetic and strong isospin-breaking corrections. The presence of a new gauge boson X alters this decomposition, and introduces an additional, irreducible contribution to O_{exp} . Therefore, one can expand O_{exp} as

$$O_{\text{exp}} = \bar{O} + O_{\text{IB}} + O_{\gamma} + O_X , \quad (5.1)$$

where \bar{O} , O_{IB} , O_{γ} denote the iso-symmetric, isospin breaking, and electromagnetic contributions respectively, whereas O_X denotes the possible NP contribution. The matching procedure is, $O_{\text{exp}} = (\mathcal{S})^{[O]} \langle O \rangle_{\text{lat}}$ with $[O]$ being the energy dimension of O . In BMW20 [21],

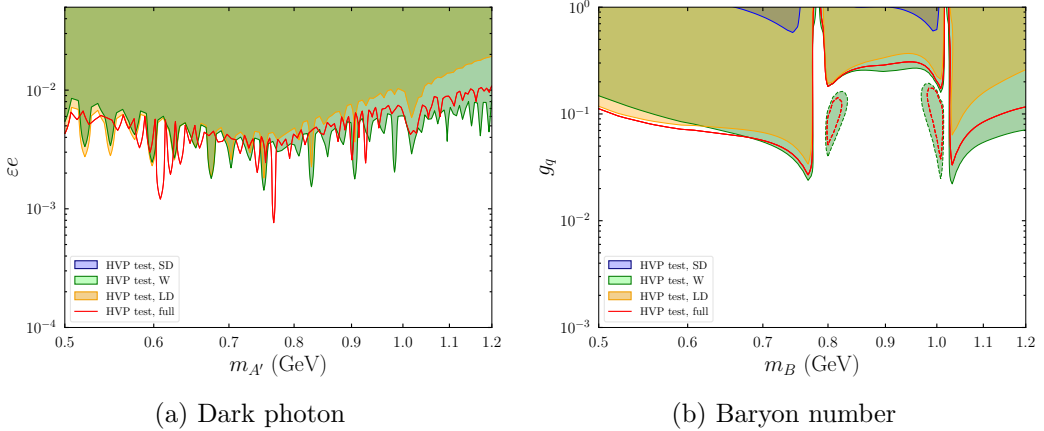


Figure 10: Bounds from fine grained HVP test for A' (Fig. 10a) and B (Fig. 10b) considering $(a_\mu^{\text{HVP}})^{\text{DD}} = (a_\mu^{\text{HVP}})^{\text{lat}}$. Different colors depict the HVP tests in different windows as: blue: a_μ^{SD} using ETMC [13]; green: a_μ^{W} using BMW 24 [20], orange: a_μ^{LD} using Mainz 24 [15]; red=full HVP test (c.f. Fig. 6 and 7 respectively), whereas the solid and dashed contours show $+2\sigma$, and -2σ exclusions respectively.

the mass of Ω^- baryon ($M_{\Omega^-} = 1672.5$ MeV), is used as the physical scale setting observable.

To estimate the correction due to X , we rescale the EM contribution of M_{Ω^-} as $\delta M_X^{\Omega^-} \sim (g_d^X/e)^2 M_\gamma^{\Omega^-}$ where $M_\gamma^{\Omega^-}$ denotes the EM self energy correction of omega baryon mass which is estimated to be $< (0.4\%) M_{\Omega^-}$ [21]. As the self-energy correction to the fermion masses due to gauge bosons is logarithmic in nature, by adding a possible log correction, we obtain

$$\delta M_X^{\Omega^-} \sim \frac{(g_d^X)^2}{4\pi\alpha} M_\gamma^{\Omega^-} \ln\left(\frac{m_X^2}{\Lambda^2}\right) \sim 52 \text{ MeV} \times (g_d^X)^2, \quad (5.2)$$

where $\Lambda \sim \text{GeV}$ is some characteristic scale and we use $m_X = 600$ MeV. For $X = B$, by using $g_d^X = g_q \lesssim 0.15$, we obtain the NP correction of $\delta M_X^{\Omega^-} \sim 1$ MeV, and for $X = A'$, by using $\varepsilon = 0.1$, we get the mass correction to be of 0.05 MeV. These corrections are within 0.4% scale-setting uncertainty quoted in the BMW20 [21] estimate. Note that the other possible NP corrections to M^{Ω^-} are either of higher power of NP couplings and/or loop factor suppressed, and hence are not considered here. Also, a similar analysis can be performed for other scale setting observables, such as the pion decay constant (see [20]) as well. However, as long as the EM contribution to those scales is well within the quoted uncertainty, the NP contributions will not lead to any new errors, and thus can be safely neglected.

5.2 Fine grained HVP test

In lattice QCD, the HVP contribution to a_μ is calculated based on the integral over Euclidean time, t , of the two-point functions of quark EM current convoluted with a kernel

$\tilde{K}(t)$ as [68],

$$(a_\mu^{\text{HVP}})^{\text{lat}} = -\frac{\alpha^2}{3\pi^2} \int_0^\infty dt \tilde{K}(t) \sum_{\mu=1,2,3} \int d^3x \langle J_{\text{EM}}^\mu(\vec{x}, t) J_{\text{EM}}^\mu(0) \rangle. \quad (5.3)$$

The above integral is often separated into short distance (a_μ^{SD}), intermediate distance (a_μ^{W}), and long distance (a_μ^{LD}) contributions [67]. These are called the “window quantities”.

These window quantities can be compared with the DD HVP; hence providing us with additional information of the energy dependence of the deviations between them. In the data-driven methods, these window quantities can be obtained by adding the weight functions $\tilde{\Theta}_{\text{win}}(s)$ centered at different center of mass energy to the integral Eq. (2.1),

$$(a_\mu^{\text{HVP}})^{\text{DD}}_{\text{win}} = \frac{1}{4\pi^3} \int_{s_{\text{exp}}}^\infty ds K(s) \tilde{\Theta}_{\text{win}}(s) \sigma(e^+e^- \rightarrow \text{had})(s). \quad (5.4)$$

The explicit form of the three weight functions $\tilde{\Theta}_{\text{win}}(s)$ can be found in [69] and in Appendix C. We also summarize the current results of the window observables from different lattice groups in Table 1 in Appendix C. We find that the large deviation shows up for the intermediate and long distance regime when BaBar/KLOE results are used in the DD method compare to the lattice results, while results from CMD-3 agrees within precision with the lattice result. However, in the short-distance window, these two methods are consistent with each other.

We utilize these window observables to provide additional fine grained HVP test of our benchmark models. The fine grained HVP test is a more futuristic test. However, as many current lattice collaborations report their HVP results in different windows, this test could become more relevant. The goal of using the HVP test in various windows, is to get a more precise estimation of how new physics enters the HVP as a function of the energy, \sqrt{s} . For example, if the new gauge boson X is light ($m_X \sim 1$ GeV), it is expected to primarily affect just the long distance or the intermediate distance windows. In the presence of X , the data-driven results of these window observables modify as,

$$(\Delta a_\mu^{\text{HVP}})^{\text{win}} = \frac{1}{4\pi^3} \int_{s_{\text{th}}}^\infty ds K(s) \tilde{\Theta}_{\text{win}}(s) (\sigma^{\gamma-X}(s) + \sigma^X(s)), \quad (5.5)$$

using the discussion in Section 2.2 (c.f. Eq. (2.18)). As an illustration, in Fig. 10a and 10b, we show the bounds obtained from the fine grained HVP test for the dark photon and B model respectively, assuming the discrepancies between lattice and data-driven eventually disappear in the future. We see that for the mass range we are considering, a_μ^{SD} is the least sensitive to the new physics and yields the weakest bound. For the dark photon, the $+2\sigma$ HVP bounds from a_μ^{W} and a_μ^{LD} are comparable at $m_{A'} \lesssim 0.8$ GeV, while a_μ^{W} gives the strongest bound when $m_{A'} \gtrsim 0.8$ GeV. For the largest masses, a_μ^{W} gives a $+2\sigma$ bound on εe that is stronger by a factor of $\mathcal{O}(2)$ compared to the bound from a_μ^{LD} . None of the HVP tests give a -2σ constraint for this model. Similarly, for B , the $+2\sigma$ HVP bounds from a_μ^{W} and a_μ^{LD} are comparable at $m_B \lesssim 1$ GeV, while a_μ^{W} gives strongest bound when $m_B \gtrsim 1$ GeV. For this model, only a_μ^{W} and the full HVP test give -2σ constraints, and they are both very similar.

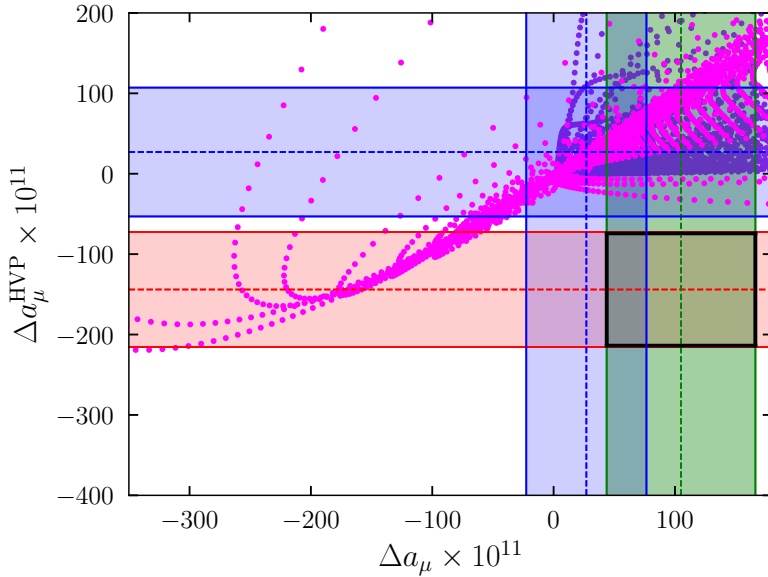


Figure 11: Plot of the two new physics contributions, Δa_μ (c.f. Eq. (2.5)) and $\Delta a_\mu^{\text{HVP}}$ (c.f. Eq. (2.4)), for $X = B$ (baryon number gauge boson) and $X = A'$ (dark photon). The zeros of the x and y axis are set at a_μ^{lat} and $(a_\mu^{\text{HVP}})^{\text{lat}}$ (from BMW 2020 [21]). The green band is the experimental world average of a_μ^{exp} [2] (with errors in quadrature with the a_μ^{lat} error) while the red band represents $(a_\mu^{\text{HVP}})_\mu^{\text{DD}}$ from TI 2020 [10] (errors in quadrature with the $(a_\mu^{\text{HVP}})^{\text{lat}}$ errors). The blue bands are a_μ and a_μ^{HVP} from the CMD-3 experiment [12, 70]. The purple and pink points depict the model prediction for the case of A' and B respectively. To satisfy both the a_μ and HVP tests by a model, upto $\pm 1\sigma$, points must lie inside the black square.

6 Conclusions

Light and weakly coupled new physics has been extensively studied in the last few years. It is, however, in general challenging to directly search for new resonances if they dominantly couple to the hadronic sector of the SM and their masses are of the order of the QCD scale. It is interesting to note however, that indirect precision measurements provide powerful probes of these types of models. Among them are the muon anomalous magnetic moment, a_μ and the photon hadronic vacuum polarization (HVP). The latter is sensitive to new physics contribution to the cross-section for $e^+e^- \rightarrow \text{hadrons}$, which also affects several other well-measured observables such as a_μ , $\sin^2 \theta_W$ and the running of α . Two precision tests can be defined, namely the Δa_μ and the $\Delta a_\mu^{\text{HVP}}$ test. The first is a comparison between the experimental and theoretical values of the muon anomalous magnetic moment. The second tests only the HVP “part” of a_μ by comparing the result of the lattice calculation for it to the value obtained using the data-driven approach, i.e., based on a measured cross-section of $e^+e^- \rightarrow \text{hadrons}$.

In this work, we have studied the implications of the above tests to a new flavor-

universal vector, X , with mass around the GeV scale. We find that in models where the hadronic coupling, g_q , is larger than the leptonic coupling, g_ℓ , the contribution to a_μ from the X -photon mixing diagram can be as significant as the naive 1-loop diagram. In addition, the X on-shell contribution to the $e^+e^- \rightarrow$ hadrons cross-section should be subtracted in the data-driven approach for computing the photon HVP contribution to a_μ , resulting in reducing the sensitivity of a_μ to 1-loop effect of X by a factor of g_ℓ^2/g_q^2 as compared to the naive expectation. In this case, a_μ is strongly sensitive to the hadronic coupling of X , albeit a_μ being a purely leptonic quantity.

We demonstrate the above by considering two specific cases, dark photon, A' , and baryon number gauge boson, B . As a summary plot, in Fig. 11, we reconcile our two benchmark models against both the tests. We see that based on the current scenario i.e. using BMW 2020 as the lattice and Theory Initiative 2020 as the data-driven result, both the tests cannot be satisfied simultaneously, leading to a complete exclusion of these models. The data-driven HVP by Theory Initiative 2020 is obtained after averaging the $e^+e^- \rightarrow$ hadrons cross-sections measured by BaBar [25, 71], KLOE [72–74], SND [75, 76] and CMD-2 [77–79]. Another noteworthy result is the data-driven value obtained from the $e^+e^- \rightarrow$ hadrons cross-section measured by CMD-3 [11, 12], shown by the blue bands in Fig. 11. Due to a discrepancy between the CMD-3 and KLOE measurements of the $e^+e^- \rightarrow \pi^+\pi^-$ cross-section, there is an estimated 4σ tension in the corresponding HVPs. Thus, it is difficult to obtain a reliable average of the HVP from CMD-3 and Theory Initiative 2020. However, as seen in Fig. 11, the CMD-3 HVP taken in isolation is consistent with BMW 2020 (at 1σ level), and does not lead to a complete exclusion of the two aforementioned models. In addition, we pointed out that by using the on-tape BaBar and Belle data sets one can perform a direct search for B in the 3π final state in events with ISR and probe the unexplored region of the parameter space.

Acknowledgments

We gratefully acknowledge Fabio Anulli, Vladimir Druzhinin, Phoebe Hamilton, Hassan Jawahery, Evgeny Kozyrev, Frank Porter, Eugeny Solodov, and Yuki Sue for their invaluable insights and thoughtful feedback. We thank Zackaria Chacko, Tom Cohen, Anson Hook, Lorenzo Ricci, and Raman Sundrum for useful discussions. The work of KA, AB, and KP is supported by the National Science Foundation under grant number PHY2210361 and the Maryland Center for Fundamental Physics. The work of MJ is supported by the Deutsche Forschungsgemeinschaft under Germany’s Excellence Strategy EXC 2121 “Quantum Universe” — 390833306, as well as by the grant 491245950. The work of GP is supported by grants from NSF-BSF, ISF and Minerva. The work of YS is supported by grants from the NSF-BSF (grant No. 2021800), the ISF (grant No. 597/24). Finally, KA and GP are grateful to the organizers of the “Physics of this Universe” workshop (Johns Hopkins University, 2022), where the seeds of this work were planted.

A Some field theoretic proofs

In this section, we prove the various field theoretic results used in the main text. In Appendix A.1 we show that the longitudinal parts of the propagator of a massive gauge boson (in the a_μ loop) and longitudinal parts of vacuum polarization functions, do not contribute to a_μ . In Appendix A.2 we derive the renormalization scheme dependence of a_μ^X , $a_\mu^{\gamma-X}$ and a_μ^{XX} followed by a proof of the renormalization scheme independence of the sum of these quantities in Appendix A.3

A.1 Longitudinal contributions to a_μ

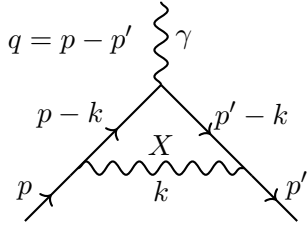


Figure 12: 1-loop $(g-2)_\mu$ with momenta labelled

The propagator of a massive gauge boson has a piece proportional to $k^\mu k^\nu$. At the 2 loop order, we also need to include propagators connected by vacuum polarization (VP) blobs. The VP tensors relevant to our computations take the forms

$$\Pi_{\gamma\gamma}^{\mu\nu}(k^2) = (k^2 - k^\mu k^\nu)g^{\mu\nu}\Pi_{\gamma\gamma}(k^2) + k^\mu k^\nu\Pi_{\gamma\gamma}^L(k^2), \quad (\text{A.1})$$

$$\Pi_{\gamma X}^{\mu\nu}(k^2) = (k^2 - k^\mu k^\nu)g^{\mu\nu}\Pi_{\gamma X}(k^2) + k^\mu k^\nu\Pi_{\gamma X}^L(k^2), \quad (\text{A.2})$$

$$\Pi_{XX}^{\mu\nu}(k^2) = ((k^2 - m_X^2)g^{\mu\nu} - k^\mu k^\nu)\Pi_{XX}(k^2) + k^\mu k^\nu\Pi_{XX}^L(k^2). \quad (\text{A.3})$$

The contribution coming from the longitudinal part of the free X propagator, i.e. the part of the propagator proportional to $k^\mu k^\nu$ in the diagram is given by (see Fig. 12)

$$\begin{aligned} a_\mu &\propto \int \frac{d^4 k}{(2\pi)^4} \bar{u}(p') \frac{\gamma^\beta (\not{p}' - \not{k} + m_\mu) \gamma^\mu (\not{p} - \not{k}) + m_\mu) \gamma^\alpha k^\alpha k^\beta}{((p - k)^2 - m_\mu^2)((p' - k)^2 - m_\mu^2)(k^2 - m_X^2)} u(p) \\ &= \int \frac{d^4 k}{(2\pi)^4} \bar{u}(p') \frac{\not{k} (\not{p}' - \not{k} + m_\mu) \gamma^\mu (\not{p} - \not{k}) + m_\mu) \not{k}}{((p - k)^2 - m_\mu^2)((p' - k)^2 - m_\mu^2)(k^2 - m_X^2)} u(p) \\ &= \int \frac{d^4 k}{(2\pi)^4} \bar{u}(p') \frac{(2(p' \cdot k) - \not{p}' \not{k}' - k^2 + m_\mu \not{k}) \gamma^\mu (2(p \cdot k) - \not{k} \not{p} - k^2 + m_\mu \not{k})}{((p - k)^2 - m_\mu^2)((p' - k)^2 - m_\mu^2)(k^2 - m_X^2)} u(p). \end{aligned} \quad (\text{A.4})$$

Using $\not{p}u(p) = m_\mu u(p)$ and $\bar{u}(p')\not{p}' = m_\mu \bar{u}(p')$, we get

$$a_\mu \propto \int \frac{d^4 k}{(2\pi)^4} \bar{u}(p') \frac{(2(p' \cdot k) - k^2) \gamma^\mu (2(p \cdot k) - k^2)}{((p - k)^2 - m_\mu^2)((p' - k)^2 - m_\mu^2)(k^2 - m_X^2)} u(p). \quad (\text{A.5})$$

Since this term is proportional only to $\bar{u}(p')\gamma_\mu u(p)$, it will not contribute to the magnetic form factor, which is proportional to $\bar{u}(p')i\sigma^{\mu\nu}(p - p')_\nu u(p)$. Note that if we want a VP

insertion in the diagram then the integrand in (A.4) now just has a VP tensor multiplied with it. This means that, for the VP pieces proportional to $k^\mu k^\nu$, our analysis falls through exactly as we showed above and we get no contribution to a_μ . Hence, any term proportional to $k^\mu k^\nu$ does not contribute to a_μ , and can be safely neglected in our computations.

A.2 2-loop calculations for a_μ and renormalization schemes

In this section, we aim to obtain analytical expressions for computing 2 loop a_μ contributions (i.e. of the type in Fig. 1b). This means we have to deal with one VP insertion for each contribution. Note that we only need to deal with the scalar parts of the VP functions i.e. $\Pi_{\gamma\gamma}$, $\Pi_{\gamma X}$ or Π_{XX} , because the remaining pieces do not contribute to a_μ as shown in Appendix A.1. Since calculating the VP functions perturbatively is not possible, we turn to using the Källén–Lehmann (KL) spectral representation

$$\frac{\Pi(k^2) - \Pi(p_0^2)}{k^2 - p_0^2} = - \int_0^\infty ds \frac{\text{Im } \Pi(s)}{\pi(k^2 - s + i\varepsilon)(s - p_0^2)} = - \int_0^\infty ds \frac{\text{Im } \bar{\Pi}(s)}{\pi(k^2 - s + i\varepsilon)(s - p_0^2)} \quad (\text{A.6})$$

$$\bar{\Pi}(k^2) = \Pi(k^2) - \text{Re } \Pi(p_0^2), \quad (\text{A.7})$$

where p_0 is an arbitrary reference momentum, $\Pi = \Pi_{\gamma\gamma}$, $\Pi_{\gamma X}$ or Π_{XX} and the bar denotes that $\Pi(k^2)$ is renormalized at p_0^2 as shown above. To relate the imaginary part of Π to a measured cross section, we use the optical theorem, which gives us the following relations for the three cross sections and the corresponding VP functions (where $\int d\Pi$ is the phase space integral)

$$\sigma^\gamma(s) = \sigma(e^+ e^- \rightarrow \gamma^* \rightarrow \text{had}) = \frac{e^4 \text{Im } \bar{\Pi}_{\gamma\gamma}(s)}{s}, \quad (\text{A.8})$$

$$\begin{aligned} \sigma^{\gamma-X}(s) &= \int d\Pi 2 \text{Re} (\mathcal{A}_{e^+ e^- \rightarrow \gamma^* \rightarrow \text{had}}(s) \mathcal{A}_{e^+ e^- \rightarrow X^* \rightarrow \text{had}}^*(s)) \\ &= 2g_\ell g_q e^2 \text{Im} \left(\frac{\bar{\Pi}_{\gamma X}(s)}{s - m_X^2 + i\epsilon} \right) = 2g_\ell g_q e^2 \text{Im}(\bar{\Pi}_{\gamma X}(s)) \frac{s - m_X^2}{(s - m_X^2)^2 + \epsilon^2}, \end{aligned} \quad (\text{A.9})$$

$$\begin{aligned} \sigma^X(s) &= \sigma(e^+ e^- \rightarrow X^* \rightarrow \text{had})(s) = g_\ell^2 g_q^2 e^2 \text{Im} \left(\frac{\bar{\Pi}_{XX}(s)}{s - m_X^2 + i\epsilon} \right) \\ &= g_\ell^2 g_q^2 e^2 \text{Im } \bar{\Pi}_{XX}(s) \frac{s - m_X^2}{(s - m_X^2)^2 + \epsilon^2}. \end{aligned} \quad (\text{A.10})$$

Note that fixing a renormalization scheme for the three VP functions also fixes the scheme for the relevant couplings i.e. we have the couplings renormalized as $e = e(p_0^2)$, $g_\ell = g_\ell(p_0^2)$, $g_q = g_q(p_0^2)$. Keeping this in mind, we can now calculate the final a_μ contributions. First, we consider the SM/photon 2-loop contribution i.e

$$a_\mu^{\gamma\gamma} = \int \frac{d^4 k}{(2\pi)^4} \frac{e^4(p_0^2) \text{Re } \bar{\Pi}_{\gamma\gamma}(k^2)}{k^2} \mathcal{F}_\mu(k) \quad (\text{A.11})$$

$$= \int \frac{d^4 k}{(2\pi)^4} \frac{e^4(p_0^2) \text{Re } (\Pi_{\gamma\gamma}(k^2) - \Pi_{\gamma\gamma}(p_0^2))}{k^2} \mathcal{F}_\mu(k), \quad (\text{A.12})$$

where $\mathcal{F}_\mu(k)$ contains all the pieces from the muon propagators and the external photon vertex in the feynmann diagram. We have used Eq. (A.1) along with the results of Appendix A.1 to get the first equality. Using Eq. (A.6) for $\Pi = \Pi_{\gamma\gamma}$ and Eq. (A.8) leads to

$$\begin{aligned} a_\mu^{\gamma\gamma} &= \int_0^\infty ds e^4(p_0^2) \frac{\text{Im}\bar{\Pi}_{\gamma\gamma}(s)}{\pi(s - p_0^2)(k^2 - s)} \int \frac{d^4 k}{(2\pi)^4} \frac{k^2 - p_0^2}{k^2} \mathcal{F}_\mu(k) \\ &= \int_0^\infty ds e^4(p_0^2) \frac{\text{Im}\bar{\Pi}_{\gamma\gamma}(s)}{\pi s} \frac{d^4 k}{(2\pi)^4} \left(\frac{1}{(s - p_0^2)k^2} + \frac{1}{s(k^2 - s)} - \frac{1}{sk^2} \right) \mathcal{F}_\mu(k) \\ &= \frac{1}{4\pi^3} \int_0^\infty ds \sigma^\gamma(s) \left(K(s) + \frac{p_0^2}{s - p_0^2} K(0) \right), \end{aligned} \quad (\text{A.13})$$

where we have used the definiton of the kernel function $K(s)$ to get the last equality. Moving on to the BSM contributions, using Eq. (A.2) along with the results of Appendix A.1, we get

$$a_\mu^{\gamma-X} = \int \frac{d^4 k}{(2\pi)^4} \frac{2e^2 g_q g_\ell \bar{\Pi}_{\gamma X}(k^2) k^2}{k^2(k^2 - m_X^2)} \mathcal{F}_\mu(k) = \int \frac{d^4 k}{(2\pi)^4} \frac{2e^2 g_q g_\ell \bar{\Pi}_{\gamma X}(k^2)}{(k^2 - m_X^2)} \mathcal{F}_\mu(k), \quad (\text{A.14})$$

which upon using Eq. (A.6) for $\Pi_{\gamma X}$ leads to

$$\begin{aligned} a_\mu^{\gamma-X} &= - \int \frac{d^4 k}{(2\pi)^4} \int_0^\infty ds \frac{2e^2 g_\ell g_q \text{Im}(\bar{\Pi}_{\gamma X}(s))}{\pi(k^2 - s)(s - p_0^2)} \frac{k^2 - p_0^2}{(k^2 - m_X^2)} \mathcal{F}_\mu(k) \\ &= \int_0^\infty ds \frac{2e^2 g_\ell g_q \text{Im}(\bar{\Pi}_{\gamma X}(s))}{(s - m_X^2)(s - p_0^2)} \int \frac{d^4 k}{(2\pi)^4} \frac{1}{\pi} \left(\frac{s - p_0^2}{k^2 - s} + \frac{p_0^2 - m_X^2}{k^2 - m_X^2} \right) \mathcal{F}_\mu(k). \end{aligned}$$

Finally, using Eq. (A.9) in the off-shell limit i.e. $s \neq m_X^2$ leads to the simplification

$$a_\mu^{\gamma-X} = \frac{1}{4\pi^3} \int_0^\infty ds \sigma^{\gamma-X}(s) \left(K(s) + \frac{p_0^2 - m_X^2}{s - p_0^2} K(m_X^2) \right) \quad (\text{A.15})$$

$$K_{\gamma-X}(s) = K(s) + \frac{p_0^2 - m_X^2}{s - p_0^2} K(m_X^2), \quad (\text{A.16})$$

where $K_{\gamma-X}(s)$ can be viewed as the kernel for $a_\mu^{\gamma-X}$. Similarly, we can also compute the XX contribution. Using Eq. (A.3) along with the results of Appendix A.1 leads to

$$a_\mu^{XX} = \int \frac{d^4 k}{(2\pi)^4} \frac{g_q^2 g_\ell^2 \bar{\Pi}_{XX}(k^2 - m_X^2)}{(k^2 - m_X^2)^2} \mathcal{F}_\mu(k) = \int \frac{d^4 k}{(2\pi)^4} \frac{g_q^2 g_\ell^2 \bar{\Pi}_{XX}}{(k^2 - m_X^2)} \mathcal{F}_\mu(k). \quad (\text{A.17})$$

Now using Eq. (A.6) for Π_{XX} gives

$$\begin{aligned} a_\mu^{XX} &= - \int \frac{d^4 k}{(2\pi)^4} \int_0^\infty ds \frac{g_\ell^2 g_q^2 \text{Im}(\bar{\Pi}_{XX}(s))}{\pi(k^2 - s)(s - p_0^2)} \frac{k^2 - p_0^2}{(k^2 - m_X^2)} \mathcal{F}_\mu(k) \\ &= \frac{1}{4\pi^3} \int_0^\infty ds \frac{g_\ell^2 g_q^2 \text{Im}(\bar{\Pi}_{XX}(s))}{(s - m_X^2)(s - p_0^2)} ((s - p_0^2)K(s) + (p_0^2 - m_X^2)K(m_X^2)). \end{aligned}$$

Finally, using Eq. (A.10) in the off-shell limit

$$a_\mu^{XX} = \frac{1}{4\pi^3} \int_0^\infty ds \sigma^{\text{off-shell } X}(s) \left(K(s) + \frac{p_0^2 - m_X^2}{s - p_0^2} K(m_X^2) \right) \quad (\text{A.18})$$

$$K_{XX}(s) = K(s) + \frac{p_0^2 - m_X^2}{s - p_0^2} K(m_X^2), \quad (\text{A.19})$$

where $K_{XX}(s)$ can be viewed as the kernel for a_μ^{XX} . Therefore, we see that the expressions of the 2 loop contributions to a_μ depend on the reference momentum p_0 . Importantly, we see that

$$a_\mu^{\gamma\gamma} = (a_\mu^{\text{HVP}})_{e^+e^- \rightarrow \text{had}}^{\gamma\gamma} \quad \text{for } p_0^2 = 0, \quad (\text{A.20})$$

$$a_\mu^{\gamma-X} = (a_\mu^{\text{HVP}})_{e^+e^- \rightarrow \text{had}}^{\gamma-X} \quad \text{for } p_0^2 = m_X^2, \quad (\text{A.21})$$

$$a_\mu^{XX} = (a_\mu^{\text{HVP}})_{e^+e^- \rightarrow \text{had}}^{XX} \quad \text{for } p_0^2 = m_X^2, \quad (\text{A.22})$$

i.e. the a_μ contributions exactly match the HVP contributions for particular scheme choices. These choices simplify things immensely since we just get $K_{\gamma-X}(s) = K_{XX}(s) = K(s)$ and so, these are the ones that we follow in this paper. Naively, this might seem that we have a dependence on the renormalization scheme for physical observables. However, these contributions individually are not physical. One must keep in mind that the 1-loop contributions a_μ^γ and a_μ^X , due to their dependence on e^2 and g_ℓ^2 , are also renormalization scheme dependent. As we show in the next section, it is the sum of the 1-loop and 2-loop contributions that is independent of the choice of p_0 and therefore, is physical.

A.3 Renormalization scheme independence of a_μ

First, we consider the SM contributions. We start by defining

$$a_\mu^{\gamma\gamma}(p_0^2) = a_\mu^{\gamma\gamma} \quad \text{for arbitrary } p_0^2, \quad (\text{A.23})$$

$$a_\mu^{\gamma\gamma}(0) = a_\mu^{\gamma\gamma} \quad \text{for } p_0^2 = 0 \text{ scheme.} \quad (\text{A.24})$$

The running of the electric charge is given by

$$\alpha(p_0^2) = \frac{\alpha(0)}{1 - 4\pi\alpha(0)\text{Re}(\Pi_{\gamma\gamma}(p_0^2) - \Pi_{\gamma\gamma}(0))}. \quad (\text{A.25})$$

This gives us

$$\begin{aligned} a_\mu^\gamma(p_0^2) &= \frac{\alpha(p_0^2)}{2\pi} = \frac{\alpha}{2\pi} + 2\alpha^2(0)\text{Re}(\Pi_{\gamma\gamma}(p_0^2) - \Pi_{\gamma\gamma}(0)), \\ a_\mu^{\gamma\gamma}(p_0^2) &= \int \frac{d^4 k}{(2\pi)^4} \frac{e^4(p_0^2)\text{Re}(\Pi_{\gamma\gamma}(k^2) - \Pi_{\gamma\gamma}(p_0^2))}{k^2} \mathcal{F}_\mu(k) \\ &= \int \frac{d^4 k}{(2\pi)^4} \frac{e^4(p_0^2)\text{Re}(\Pi_{\gamma\gamma}(k^2) - \Pi_{\gamma\gamma}(0))}{k^2} \mathcal{F}_\mu(k) \\ &\quad + \text{Re}(\Pi_{\gamma\gamma}(0^2) - \Pi_{\gamma\gamma}(p_0^2)) \int \frac{d^4 k}{(2\pi)^4} e^4(p_0^2) \frac{1}{k^2} \mathcal{F}_\mu(k) \\ &= a_\mu^{\gamma\gamma}(0) - 2\alpha^2(0)\text{Re}(\Pi_{\gamma\gamma}(p_0^2) - \Pi_{\gamma\gamma}(0)) + \mathcal{O}(\Pi_{\gamma\gamma}^2), \end{aligned} \quad (\text{A.26})$$

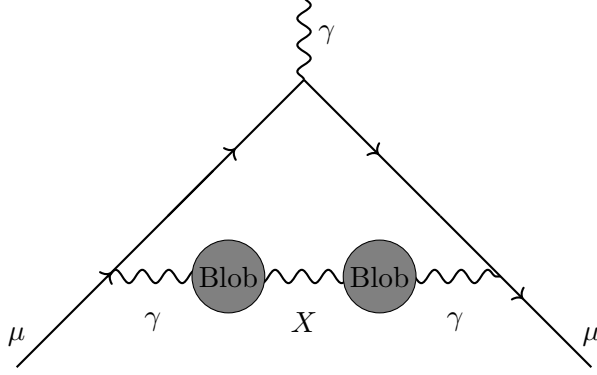


Figure 13: $\gamma - X - \gamma$ contribution to $g - 2$

where $\mathcal{O}(\Pi_{\gamma\gamma}^2)$ is the higher order contribution involving 2 VP blobs. Combining everything

$$a_\mu^\gamma(p_0^2) + a_\mu^{\gamma\gamma}(p_0^2) = a_\mu^\gamma(0) + a_\mu^{\gamma\gamma}(0) . \quad (\text{A.27})$$

Hence, the SM 1-loop + 2-loop a_μ contributions indeed turn out to be renormalization scheme independent. For the BSM contributions, we only consider the running of g_ℓ to keep the proof brief. Since the running of g_ℓ proceeds through $\gamma - X$ mixing at the leading loop order, we only need to focus on the $\gamma - X$ and 1-loop X contributions to a_μ . The running of g_ℓ through $\gamma - X$ mixing is given by:

$$g_\ell(m_X^2) = g_\ell(p_0^2) + e^2 g_q \text{Re}(\Pi_{\gamma X}(m_X^2) - \Pi_{\gamma X}(p_0^2)) + \mathcal{O}(\Pi^2) . \quad (\text{A.28})$$

We make the notations below for the arguments that follow:

$$a_\mu^X(p_0^2) = a_\mu^X \text{ for arbitrary } p_0^2 , \quad (\text{A.29})$$

$$a_\mu^X(m_X^2) = a_\mu^X \text{ for } p_0^2 = m_X^2 , \quad (\text{A.30})$$

$$a_\mu^{\gamma-X}(p_0^2) = a_\mu^{\gamma-X} \text{ for arbitrary } p_0^2 , \quad (\text{A.31})$$

$$a_\mu^{\gamma-X}(m_X^2) = a_\mu^{\gamma-X} \text{ for } p_0^2 = m_X^2 , \quad (\text{A.32})$$

$$a_\mu^{\gamma-X-\gamma}(p_0^2) = a_\mu^{\gamma-X-\gamma} \text{ for arbitrary } p_0^2 , \quad (\text{A.33})$$

$$a_\mu^{\gamma-X-\gamma}(m_X^2) = a_\mu^{\gamma-X-\gamma} \text{ for } p_0^2 = m_X^2 , \quad (\text{A.34})$$

where the $\gamma - X - \gamma$ contribution comes from the diagram shown in Fig. 13. We have:

$$a_\mu^{\gamma-X}(p_0^2) = \int \frac{d^4 k}{(2\pi)^4} \frac{2e^2 g_\ell(p_0^2) g_q \text{Re}(\Pi_{\gamma X}(k^2) - \Pi_{\gamma X}(p_0^2))}{(k^2 - m_X^2)} \mathcal{F}_\mu(k) \quad (\text{A.35})$$

$$\begin{aligned} &= \int \frac{d^4 k}{(2\pi)^4} \frac{2e^2 g_\ell(p_0^2) g_q \text{Re}(\Pi_{\gamma X}(k^2) - \Pi_{\gamma X}(m_X^2))}{(k^2 - m_X^2)} \mathcal{F}_\mu(k) \\ &+ 2e^2 g_\ell(p_0^2) g_q \text{Re}(\Pi_{\gamma X}(m_X^2) - \Pi_{\gamma X}(p_0^2)) 4\pi K(m_X^2) \end{aligned} \quad (\text{A.36})$$

$$\begin{aligned}
&= \int \frac{d^4 k}{(2\pi)^4} \frac{2e^2 g_\ell(m_X^2) g_q \operatorname{Re}(\Pi_{\gamma X}(k^2) - \Pi_{\gamma X}(m_X^2))}{(k^2 - m_X^2)} \mathcal{F}_\mu(k) \\
&- \int \frac{d^4 k}{(2\pi)^4} \frac{2e^4 g_q^2 (\operatorname{Re}(\Pi_{\gamma X}(k^2) - \Pi_{\gamma X}(m_X^2))) (\operatorname{Re}(\Pi_{\gamma X}(m_X^2) - \Pi_{\gamma X}(p_0^2)))}{(k^2 - m_X^2)} \mathcal{F}_\mu(k) \\
&+ 2e^2 g_\ell(p_0^2) g_q \operatorname{Re}(\Pi_{\gamma X}(m_X^2) - \Pi_{\gamma X}(p_0^2)) 4\pi K(m_X^2) \tag{A.37}
\end{aligned}$$

$$\begin{aligned}
&= a_\mu^{\gamma-X}(m_X^2) - \int \frac{d^4 k}{(2\pi)^4} \frac{2e^4 g_q^2 (\operatorname{Re}(\Pi_{\gamma X}(k^2) - \Pi_{\gamma X}(m_X^2))) (\operatorname{Re}(\Pi_{\gamma X}(m_X^2) - \Pi_{\gamma X}(p_0^2)))}{(k^2 - m_X^2)} \mathcal{F}_\mu(k) \\
&+ 2e^2 g_\ell(p_0^2) g_q \operatorname{Re}(\Pi_{\gamma X}(m_X^2) - \Pi_{\gamma X}(p_0^2)) 4\pi K(m_X^2) . \tag{A.38}
\end{aligned}$$

Note that, we use Eq. (2.6) to go from Eq. (A.35) to Eq. (A.36) and Eq. (A.28) to obtain Eq. (A.37) from Eq. (A.36). This gives the total a_μ contribution upto 1 VP insertion:

$$\begin{aligned}
a_\mu^X(p_0^2) + a_\mu^{\gamma-X}(p_0^2) &= \frac{1}{4\pi^2} K(m_X^2) (g_\ell^2(p_0^2) + 2e^2 g_\ell(p_0^2) g_q \operatorname{Re}(\Pi_{\gamma X}(m_X^2) - \Pi_{\gamma X}(p_0^2))) + a_\mu^{\gamma-X}(m_X^2) \\
&- \int \frac{d^4 k}{(2\pi)^4} \frac{2e^4 g_q^2 (\operatorname{Re}(\Pi_{\gamma X}(k^2) - \Pi_{\gamma X}(m_X^2))) (\operatorname{Re}(\Pi_{\gamma X}(m_X^2) - \Pi_{\gamma X}(p_0^2)))}{(k^2 - m_X^2)} \mathcal{F}_\mu(k) \tag{A.39} \\
&= \frac{1}{4\pi^2} K(m_X^2) \left(g_\ell^2(m_X^2) + a_\mu^{\gamma-X}(m_X^2) - \int \frac{d^4 k}{(2\pi)^4} \frac{e^4 g_q^2 (\operatorname{Re}(\Pi_{\gamma X}(m_X^2) - \Pi_{\gamma X}(p_0^2)))^2}{(k^2 - m_X^2)} \right) \mathcal{F}_\mu(k) \\
&- \int \frac{d^4 k}{(2\pi)^4} \frac{2e^4 g_q^2 (\operatorname{Re}(\Pi_{\gamma X}(k^2) - \Pi_{\gamma X}(m_X^2))) (\operatorname{Re}(\Pi_{\gamma X}(m_X^2) - \Pi_{\gamma X}(p_0^2)))}{(k^2 - m_X^2)} \mathcal{F}_\mu(k) \\
&= a_\mu^X(m_X^2) + a_\mu^{\gamma-X}(m_X^2) - \int \frac{d^4 k}{(2\pi)^4} \frac{e^4 g_q^2 (\operatorname{Re}(\Pi_{\gamma X}(m_X^2) - \Pi_{\gamma X}(p_0^2)))^2}{(k^2 - m_X^2)} \mathcal{F}_\mu(k) \\
&- \int \frac{d^4 k}{(2\pi)^4} \frac{2e^4 g_q^2 (\operatorname{Re}(\Pi_{\gamma X}(k^2) - \Pi_{\gamma X}(m_X^2))) (\operatorname{Re}(\Pi_{\gamma X}(m_X^2) - \Pi_{\gamma X}(p_0^2)))}{(k^2 - m_X^2)} \mathcal{F}_\mu(k) . \tag{A.40}
\end{aligned}$$

where we use Eq. (2.6) to massage the first term of Eq. (A.39) to the first term of Eq. (A.40). Now we also include the 2 VP insertions contribution given by:

$$\begin{aligned}
a_\mu^{\gamma-X-\gamma}(p_0^2) &= \int \frac{d^4 k}{(2\pi)^4} \frac{e^4 g_q^2 (\operatorname{Re}(\Pi_{\gamma X}(k^2) - \Pi_{\gamma X}(0)))^2}{(k^2 - m_X^2)} \mathcal{F}_\mu(k) \\
&= \int \frac{d^4 k}{(2\pi)^4} \frac{e^4 g_q^2 (\operatorname{Re}(\Pi_{\gamma X}(k^2) - \Pi_{\gamma X}(m_X^2)))^2}{(k^2 - m_X^2)} \mathcal{F}_\mu(k) \\
&+ \int \frac{d^4 k}{(2\pi)^4} \frac{e^4 g_q^2 (\operatorname{Re}(\Pi_{\gamma X}(m_X^2) - \Pi_{\gamma X}(0)))^2}{(k^2 - m_X^2)} \mathcal{F}_\mu(k) \\
&+ \int \frac{d^4 k}{(2\pi)^4} \frac{2e^4 g_q^2 (\operatorname{Re}(\Pi_{\gamma X}(k^2) - \Pi_{\gamma X}(m_X^2))) (\operatorname{Re}(\Pi_{\gamma X}(m_X^2) - \Pi_{\gamma X}(0)))}{(k^2 - m_X^2)} \mathcal{F}_\mu(k) \\
&= a_\mu^{\gamma-X-\gamma}(m_X^2) + \int \frac{d^4 k}{(2\pi)^4} \frac{e^4 g_q^2 (\operatorname{Re}(\Pi_{\gamma X}(m_X^2) - \Pi_{\gamma X}(0)))^2}{(k^2 - m_X^2)} \mathcal{F}_\mu(k) \\
&+ \int \frac{d^4 k}{(2\pi)^4} \frac{2e^4 g_q^2 (\operatorname{Re}(\Pi_{\gamma X}(k^2) - \Pi_{\gamma X}(m_X^2))) (\operatorname{Re}(\Pi_{\gamma X}(m_X^2) - \Pi_{\gamma X}(0)))}{(k^2 - m_X^2)} \mathcal{F}_\mu(k) . \tag{A.41}
\end{aligned}$$

This finally leads to:

$$a_\mu^X(p_0^2) + a_\mu^{\gamma-X}(p_0^2) + a_\mu^{\gamma-X-\gamma}(p_0^2) = a_\mu^X(m_X^2) + a_\mu^{\gamma-X}(m_X^2) + a_\mu^{\gamma-X-\gamma}(m_X^2). \quad (\text{A.42})$$

Hence, we have shown the sum of the 1-loop and 2-loop BSM contributions is also scheme independent (we have shown it up to 2 VP insertions but one can continue to check this for higher orders).

B Further explorations of the tests and parameter space

B.1 Contour plots for the a_μ and HVP tests

In this section, we address the value added by the a_μ and HVP test individually, before we combine them with existing constraints in the next section. In Fig. 14a we focus on the lattice a_μ test by plotting the contours for $\Delta a_\mu = a_\mu^B + a_\mu^{\gamma-B}$ in the plane of g_ℓ/g_q and m_B . The dashed black lines show the contours for $\Delta a_\mu = a_\mu^{\text{exp}} - a_\mu^{\text{lat}} \pm 2\sigma$, and the solid colored lines show contours for some fixed values of Δa_μ . In Fig. 14b we focus on the data-driven a_μ test by plotting contours for $\Delta a_\mu = a_\mu^B - (a_\mu^{\text{HVP}})_{e^+e^- \rightarrow \text{had}}^B$ in the plane of g_ℓ/g_q and m_B . In Fig. 15, we focus on the HVP by plotting contours for $\Delta a_\mu^{\text{HVP}} = a_\mu^{BB} + a_\mu^{\gamma-B}$. Fig. 15a is for the futuristic case where $\Delta a_\mu = (a_\mu^{\text{HVP}})^{\text{DD}} = (a_\mu^{\text{HVP}})^{\text{lat}}$ while Fig. 15b is for the case where $(a_\mu^{\text{HVP}})^{\text{DD}} = (a_\mu^{\text{HVP}})^{\text{TI}}$. The dashed black lines show the contours for $\Delta a_\mu = (a_\mu^{\text{HVP}})^{\text{DD}} - (a_\mu^{\text{HVP}})^{\text{lat}} \pm 2\sigma$, and the solid colored lines again show contours for some fixed values of $\Delta a_\mu^{\text{HVP}}$. The gray regions, in both the plots, are excluded by the respective tests. Since, the experimental, lattice and data-driven numbers (the differences

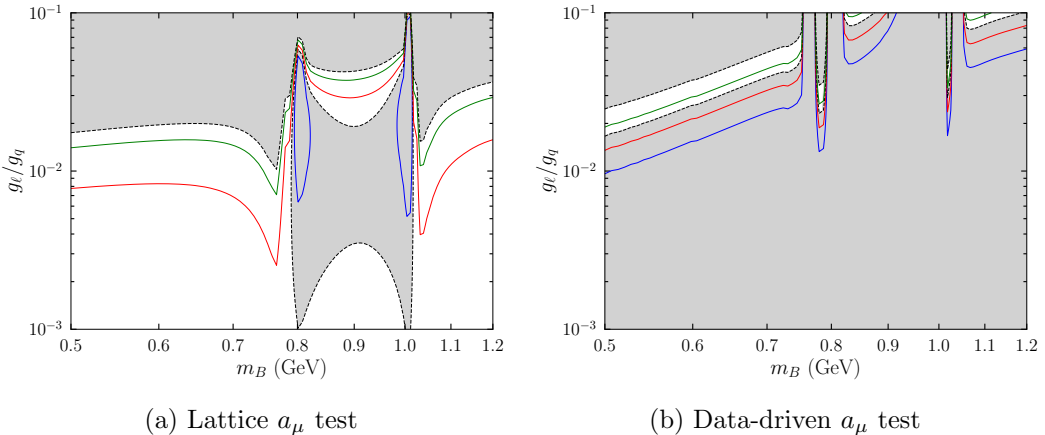


Figure 14: Contour plots for Δa_μ , in units of 10^{-11} , in the parameter space of g_ℓ/g_q vs. m_B , for the B gauge boson model. Here we have fixed $g_q = 0.15$. (Left:) We consider the lattice a_μ test (c.f. Eq. (2.14)). The blue, red and green contour lines are for $\Delta a_\mu = -100, 50, 150$. (Right:) We consider the data-driven a_μ test (c.f. Eq. (2.15)). The blue, red and green contour lines are for $\Delta a_\mu = 50, 100, 200$. In both figures, the black dashed lines represent the contours for $\Delta a_\mu = \text{current difference} \pm 2\sigma$, and hence the gray regions are currently excluded by the corresponding a_μ tests.

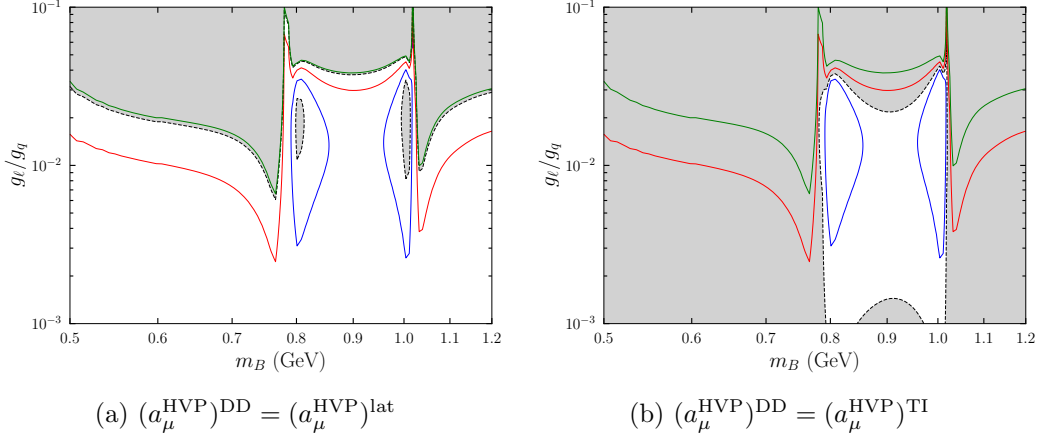


Figure 15: Contour plots of $\Delta a_\mu^{\text{HVP}}$ (see Eq. (2.4)), in units of 10^{-11} , in the parameter space of g_ℓ/g_q vs. m_B , for the B gauge boson model. Here we have fixed $g_q = 0.15$. (Left:) We consider a futuristic conservative scenario of $(a_\mu^{\text{HVP}})^{\text{DD}} = (a_\mu^{\text{HVP}})^{\text{lat}}$. (Right:) We consider the current status of $(a_\mu^{\text{HVP}})^{\text{DD}} = (a_\mu^{\text{HVP}})^{\text{lat}} - 144$ without the B contribution. The blue, red and green contour lines are for $\Delta a_\mu^{\text{HVP}} = -50, 50, 150$ while the black dashed lines represent the contours for $\Delta a_\mu = \pm 2\sigma$, and hence, the gray regions are excluded by the HVP test.

between them and their errors) can change but the various contours remain fixed, these plots give an idea about how the contributions from B can be excluded/included if these numbers shift. We already see that we rule out a lot of parameter space just by considering these two tests. In the most extreme case i.e. when we use Fig. 15b, we rule out almost all of the parameter space through a single test.

B.2 Plots for different g_ℓ/g_q for the B boson

In this section, we provide plots for the baryon number gauge boson, i.e. g_q vs. m_B for some additional values of g_q/g_ℓ (which we denote by r here). We start by considering the current scenario i.e. taking the TI 2020 number for the data-driven HVP. Using this number, we perform the HVP test along with the data-driven a_μ test. We do it for two values of r , namely $r = 0.05$ and $r = 0.005$ in Fig. 16a and 18a respectively. We see that for both the a_μ and HVP tests, we require New Physics(NP) at the $\pm 2\sigma$ level. Due to the resonant B term being positive and large (see Eq. (2.13)) $\Delta a_\mu^{\text{HVP}}$ being negative in the HVP test, most of the points in the parameter space are excluded. Only points close to the hadronic resonances manage to make $a_\mu^{\gamma-B}$ large and negative enough to satisfy the HVP test. With the data-driven a_μ test, we still exclude most of the parameter space due to the cancellations between the $(a_\mu^{\text{HVP}})_{e^+e^- \rightarrow \text{had}}^B$ and a_μ^B in Eq. (2.15). Since both these quantities depend on g_ℓ^2 , the numbers for $\pm 2\sigma$ bounds on g_q from the data-driven a_μ test become larger with increasing r (compare Fig. 7, 16a and 18a) and thus the bounds are weaker(since existing constraints already require $g_q \leq 0.15$).

To examine the effects of switching the sign of $a_\mu^{\gamma-B}$, we consider the same r values but of opposite signs in Fig. 16b and 18b. Since the a_μ test only depends on g_ℓ^2 , the sign flip

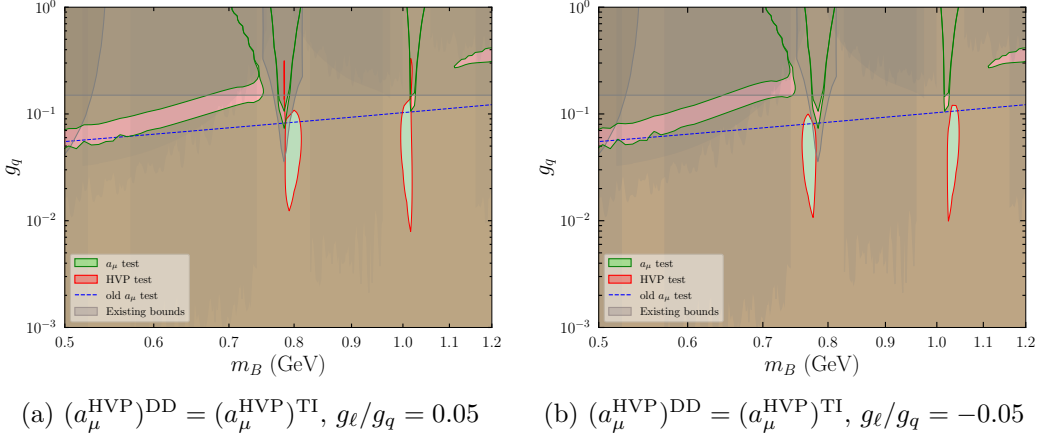


Figure 16: Parameter space of the quark coupling g_q as the function of the mass of B mass (m_B) for $g_\ell/g_q = 0.05$ (Fig. 16a) and $g_\ell/g_q = -0.05$ (Fig. 16b). In this plot, we consider the data-driven a_μ test (c.f. Eq. (2.15)). Both for the HVP test (c.f. Eq. (2.4)) and the a_μ , we take TI 2020 as the data driven value. The colour scheme is the same as the main text.

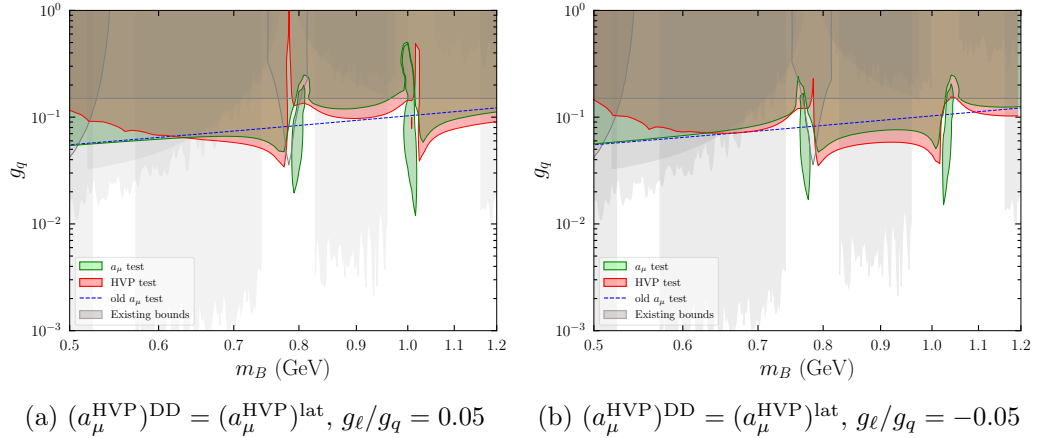


Figure 17: Parameter space of the quark coupling g_q as the function of the mass of B mass (m_B) for $g_\ell/g_q = 0.05$ (Fig. 17a) and $g_\ell/g_q = -0.05$ (Fig. 17b). We perform the lattice a_μ test (c.f. Eq. (2.14)) by taking the BMW result as the SM contribution. For the HVP test (c.f. Eq. (2.4)), we consider a futuristic conservative possibility of the central values of the data driven HVP and the lattice result to match with each other within their respective error bars. The colour scheme is the same as the main text.

does not affect it. Due to $a_\mu^{\gamma-B}$ changing signs, we see that there are no regions satisfying the HVP tests for both signs for a particular r . Another signature of the sign flip is that the regions satisfying the HVP tests are on the opposite side of the hadronic resonances (compared to the positive r cases).

In Fig. 17a and 19a, we perform the lattice a_μ test (c.f. Eq. (2.14)) for $g_\ell/g_q = 0.05$ and 0.005 respectively. As mentioned in Sec. 4.2, for the HVP test, we consider the futuristic

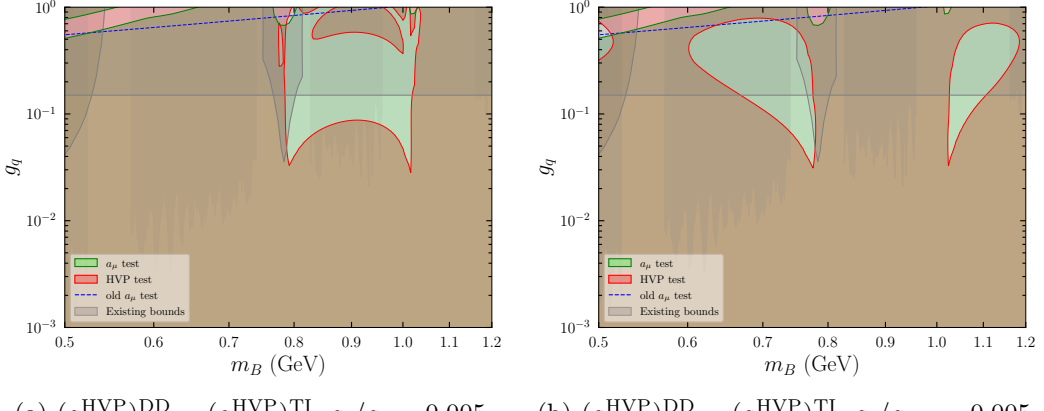


Figure 18: Parameter space of the quark coupling g_q as the function of the mass of B mass (m_B) for $g_\ell/g_q = 0.005$ (Fig. 18a) and $g_\ell/g_q = -0.005$ (Fig. 18b). Rest matches Fig. 16.

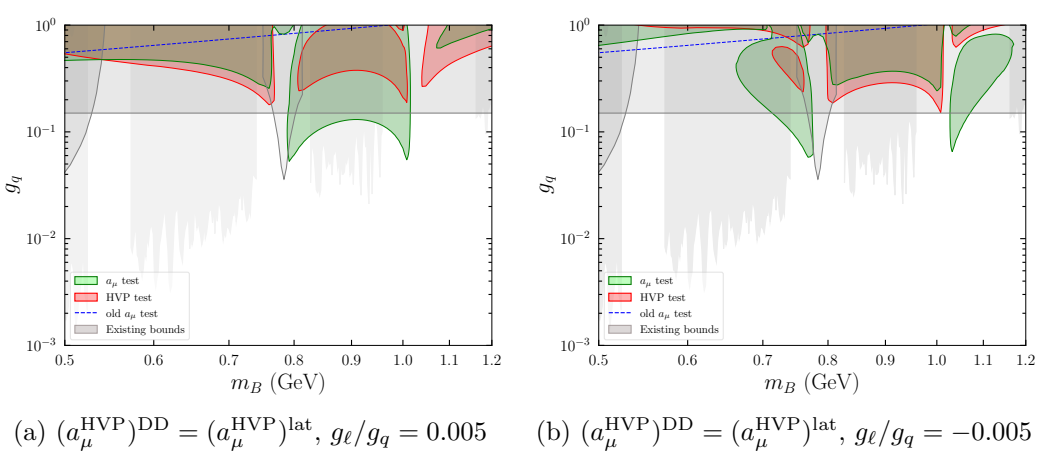


Figure 19: Parameter space of the quark coupling g_q as the function of the mass of B mass (m_B) for $g_\ell/g_q = 0.005$ (Fig. 18a) and $g_\ell/g_q = -0.005$ (Fig. 18b). Rest matches Fig. 17.

assumption, $(a_\mu^{\text{HVP}})^{\text{DD}} = (a_\mu^{\text{HVP}})^{\text{lat}}$. For the choice of the lattice a_μ test, no NP is required to satisfy either of the tests within the 2σ value. making $g_\ell, g_q \rightarrow 0$ consistent with that choice. For this choice, both the tests depend on the $a_\mu^{\gamma-B}$ which could be of either sign, and can be large close to the ω and/or ϕ mass. Near these masses, a large but negative $a_\mu^{\gamma-B}$ can offset the positive $(a_\mu^{\text{HVP}})_{e^+e^- \rightarrow \text{had}}^B$ and a_μ^B contributions. This is the reason we see closed red curves and the closed green curves, in the $m_B \sim [0.8, 1]$ GeV region, are excluded because those obtain values below the 2σ region for the respective tests. Other regions show the parameter space which is above the 2σ value, and thus are excluded. For a positive $a_\mu^{\gamma-B}$, we see that for both the HVP and lattice a_μ test, we need to satisfy a condition which is roughly: $c_1 g_q g_\ell + c_2 g_\ell^2 < 2\sigma$, where $c_1, c_2 > 0$. Solving this equation shows that the $+2\sigma$ bound on $r = 0.005$ is the weakest and that on $r = 0.05$ is the strongest. Just like before, we consider the negative r values for these tests as well. These are shown in Fig. 17b and 19b. This time, the sign flip affects both the tests. We see that the -2σ

excluded regions for both tests are now just outside the $[0.8, 1]$ GeV region, since the $a_\mu^{\gamma^-B}$ is large there, and it flips sign. The HVP test requires $a_\mu^{\gamma^-X} + (a_\mu^{\text{HVP}})_{{e^+e^- \rightarrow \text{had}}}^X$ to lie in $[-2\sigma, 2\sigma]$. Thus, the $+2\sigma$ bound from of the HVP test becomes more stringent in the $[0.8, 1]$ GeV region, because of $a_\mu^{\gamma^-B}$ being positive (on top of $(a_\mu^{\text{HVP}})_{{e^+e^- \rightarrow \text{had}}}^B$ always being positive).

B.3 Plots of g_q vs. g_ℓ for B boson with a different m_B

In Section 4.2, we charted the parameter space of g_q and g_ℓ for B , using a fixed mass $m_B = 0.9$ GeV. Here, in Fig. 20, we present the plots for another mass, $m_B = 1.085$ GeV. In Fig. 20a and 20b we use the TI 2020 number for the data-driven HVP and perform the HVP (c.f. (2.4)) and data-driven a_μ (c.f. Eq. (2.15)) tests. Similar to the case of Section 4.2, we see that not many points satisfy the data-driven a_μ test because of the cancellation between a_μ^B and $(a_\mu^{\text{HVP}})_{{e^+e^- \rightarrow \text{had}}}^B$. We also see that because $\Delta a_\mu^{\text{HVP}}$ is very negative, we do not satisfy the HVP test as well. For this case, the HVP test is better than the a_μ test. In Fig. 20c and 20d we take the futuristic case where the lattice and data-driven HVP results are equal and perform the HVP (c.f. (2.4)) and lattice a_μ (c.f. Eq. (2.14)) tests. Here, we do not rule out arbitrarily small couplings. The HVP test fares better than the lattice a_μ test place for $g_\ell \times g_q > 0$, whereas the lattice a_μ test does slightly better for $g_\ell \times g_q < 0$.

B.4 Plots for various data-driven vs lattice HVP scenarios

In Section 4.2, we charted the parameter space of both dark photon and B boson for the futuristic case where the $(a_\mu^{\text{HVP}})^{\text{DD}} = (a_\mu^{\text{HVP}})^{\text{lat}}$. We then performed the lattice a_μ and HVP tests. To highlight the complementary nature of the two tests, we now present the results for two cases: Case A: $(a_\mu^{\text{HVP}})^{\text{DD}} = (a_\mu^{\text{HVP}})^{\text{lat}} + 1\sigma$ and Case B: $(a_\mu^{\text{HVP}})^{\text{DD}} = (a_\mu^{\text{HVP}})^{\text{lat}} - 1\sigma$. These cases do not impact the a_μ test and only the bounds from the HVP tests will change. We note that, to satisfy the HVP test within $\pm 2\sigma$, $a_\mu^{\gamma^-X} + (a_\mu^{\text{HVP}})_{{e^+e^- \rightarrow \text{had}}}^X$ has to lie in the range $[-\sigma, 3\sigma]$ and $[-3\sigma, \sigma]$ for Case A and B respectively. Since $(a_\mu^{\text{HVP}})_{{e^+e^- \rightarrow \text{had}}}^X$ is always positive, it is more difficult to satisfy the HVP test on the $+2\sigma$ side for Case B. Thus, we expect the $+2\sigma$ bounds to be stronger for this condition. However, we could have $a_\mu^{\gamma^-B}$ become negative and large (which happens for m_B near hadronic resonances). For such situations, from the allowed ranges shown above, satisfying the HVP test on the -2σ is easier if we take Case B, and thus results in weaker -2σ bounds. To further illustrate these observations, we consider the two models separately:

Dark photon: For the dark photon, we present the results in Fig. 21. We see that for Case A the HVP test bounds are completely subsumed by the lattice a_μ test bounds, while for Case B, the HVP bounds are roughly equal to the a_μ bounds.

B boson: For the B boson, we present the results in Fig. 22-27. Again, for Case A, we see that the HVP test is not much better than the lattice a_μ test for $m_B \gtrsim 0.7$ GeV. For lower masses, such as $m_B \simeq 0.5$ GeV, the a_μ bounds are stronger by $\mathcal{O}(2)$. For Case B, we obtain stronger $+2\sigma$ HVP bounds as argued before. Compared to the $+2\sigma$ HVP bounds of Case A and the a_μ bounds, the $+2\sigma$ HVP bounds for Case B can be stronger by

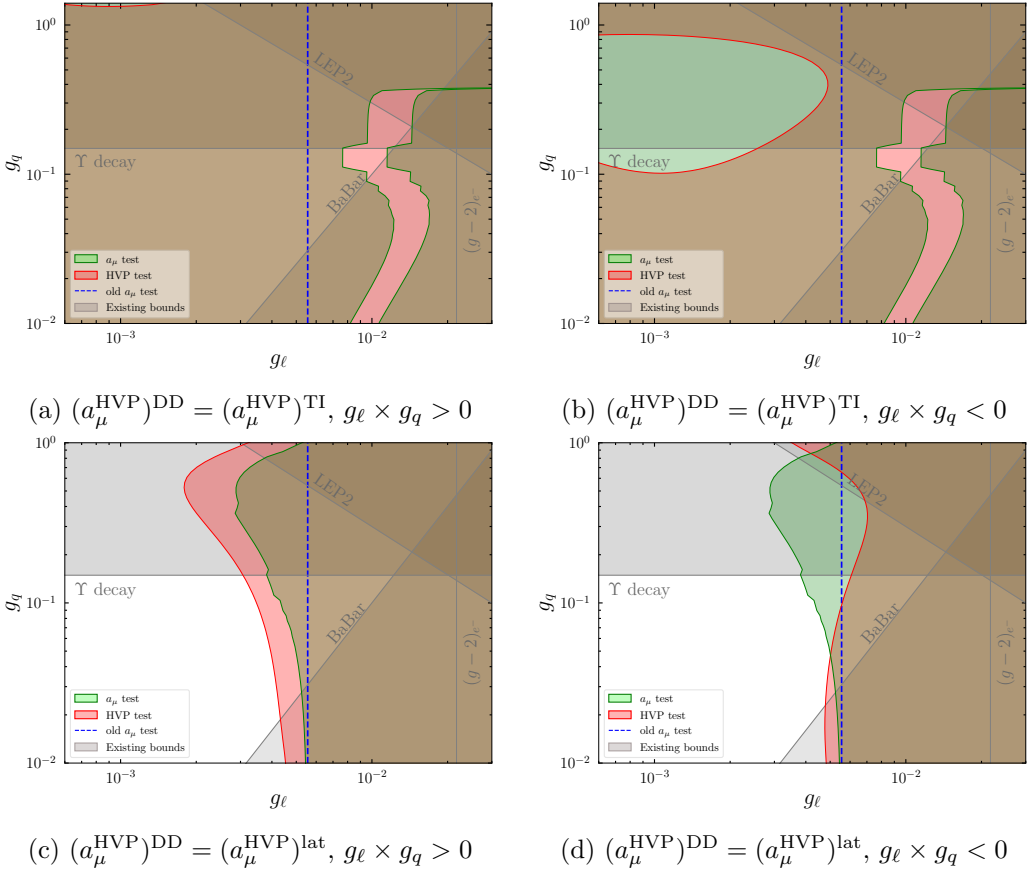


Figure 20: Plot of g_q vs g_ℓ for a fixed of $m_B = 1.085$ GeV both for positive and negative ratio. For the plots with $g_\ell \times g_q < 0$, we always consider $g_q > 0$ and plot $|g_\ell|$. In Fig. 9a and 9b, we perform the data-driven a_μ test (c.f. (2.15)) and take the TI 2020 value for the HVP test, whereas in Fig. 9c and 9d, we consider the lattice a_μ test (c.f. (2.5)) and take the data-driven HVP to be equal to the lattice result for the HVP test. The colour scheme is the same as the main text.

$\mathcal{O}(2)$. The -2σ HVP bounds for Case A are much stronger than those for Case B (where we even do not have any bounds in some cases). However, they are weaker than the -2σ a_μ bounds.

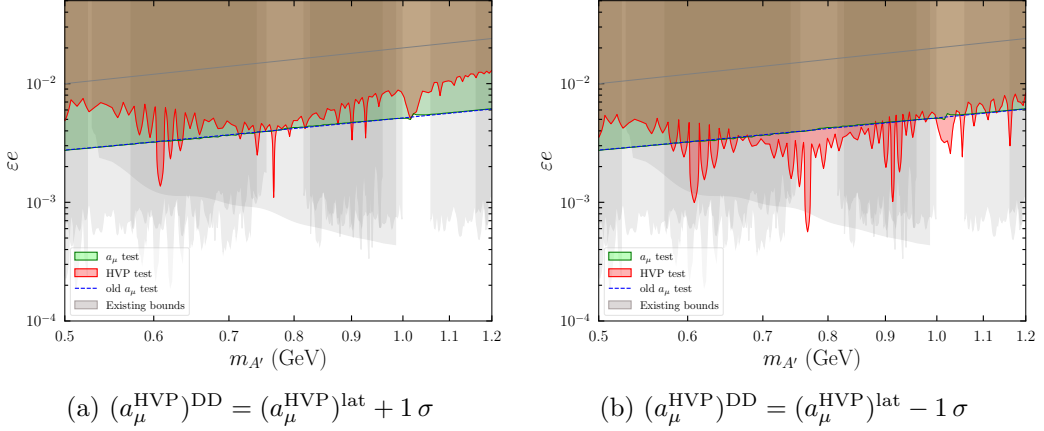


Figure 21: Parameter space of the dark photon coupling εe as a function of its mass $m_{A'}$ for the lattice a_{μ} test (c.f. Eq. (2.14)). We use BMW result for the a_{μ} test [20]. For the HVP test, we consider the possibility that $(a_{\mu}^{\text{HVP}})^{\text{DD}} = (a_{\mu}^{\text{HVP}})^{\text{lat}} + 1\sigma$ (Fig. 21a) or $(a_{\mu}^{\text{HVP}})^{\text{DD}} = (a_{\mu}^{\text{HVP}})^{\text{lat}} - 1\sigma$ (Fig. 21b). The colour scheme is the same as the main text.

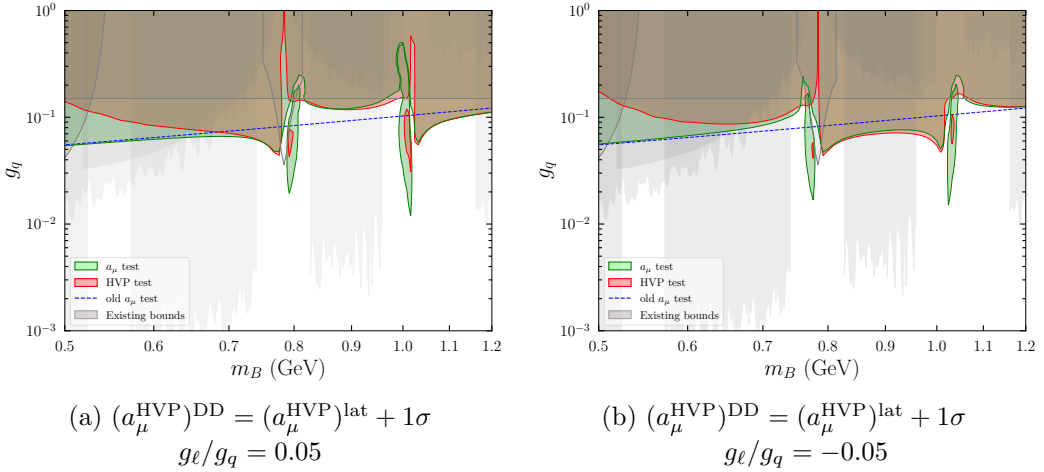


Figure 22: Parameter space of the quark coupling g_q as the function of the mass of B mass (m_B) for $g_{\ell}/g_q = 0.05$ (Fig. 22a) and $g_{\ell}/g_q = -0.05$ (Fig. 22b). We perform the lattice a_{μ} test (c.f. Eq. (2.14)) by taking the BMW result as the SM contribution. For the HVP test, we consider the possibility that $(a_{\mu}^{\text{HVP}})^{\text{DD}} = (a_{\mu}^{\text{HVP}})^{\text{lat}} + 1\sigma$. The colour scheme is the same as the main text.

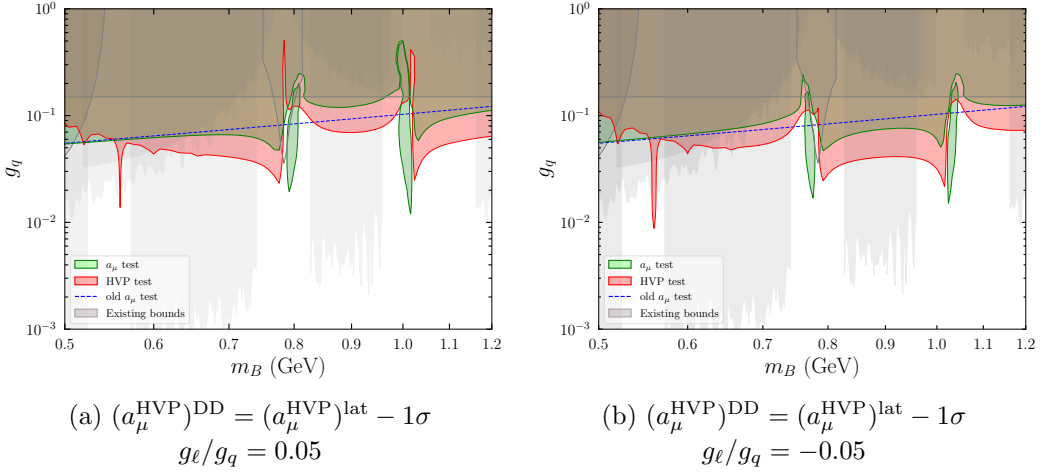


Figure 23: Parameter space of the quark coupling g_q as the function of the mass of B mass (m_B) for $g_\ell/g_q = 0.05$ (Fig. 23a) and $g_\ell/g_q = -0.05$ (Fig. 23b). We perform the lattice a_μ test (c.f. Eq. (2.14)) by taking the BMW result as the SM contribution. For the HVP test, we consider the possibility that $(a_\mu^{\text{HVP}})^{\text{DD}} = (a_\mu^{\text{HVP}})^{\text{lat}} - 1\sigma$. Rest matches Fig. 22.

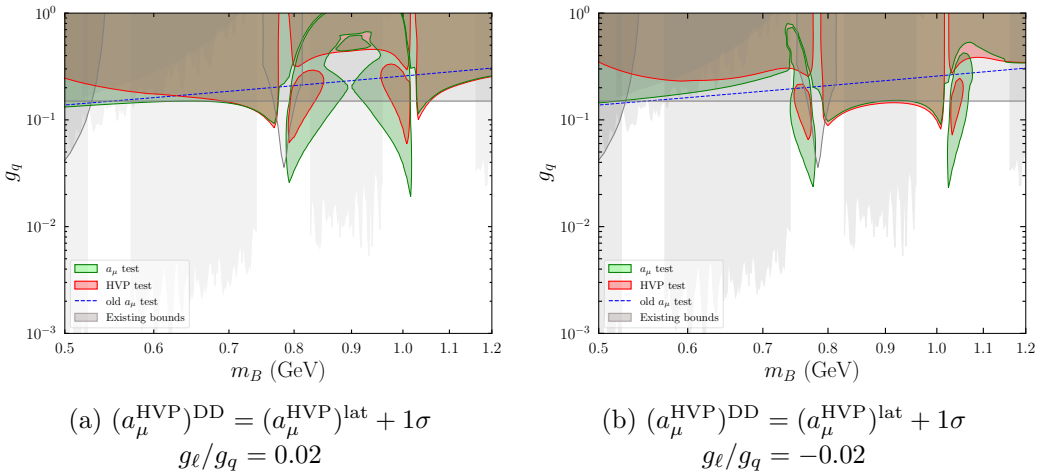


Figure 24: Parameter space of the quark coupling g_q as the function of the mass of B mass (m_B) for $g_\ell/g_q = 0.02$ (Fig. 24a) and $g_\ell/g_q = -0.02$ (Fig. 24b). We perform the lattice a_μ test (c.f. Eq. (2.14)) by taking the BMW result as the SM contribution. For the HVP test, we consider the possibility that $(a_\mu^{\text{HVP}})^{\text{DD}} = (a_\mu^{\text{HVP}})^{\text{lat}} + 1\sigma$. Rest matches Fig. 22.

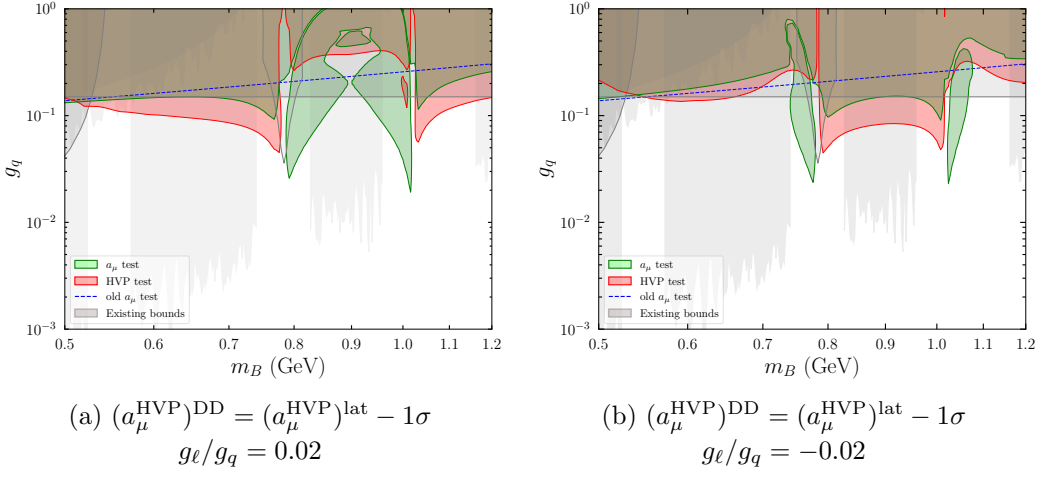


Figure 25: Parameter space of the quark coupling g_q as the function of the mass of B mass (m_B) for $g_\ell/g_q = 0.02$ (Fig. 25a) and $g_\ell/g_q = -0.02$ (Fig. 25b). We perform the lattice a_μ test (c.f. Eq. (2.14)) by taking the BMW result as the SM contribution. For the HVP test, we consider the possibility that $(a_\mu^{\text{HVP}})^{\text{DD}} = (a_\mu^{\text{HVP}})^{\text{lat}} - 1\sigma$. Rest matches Fig. 22.

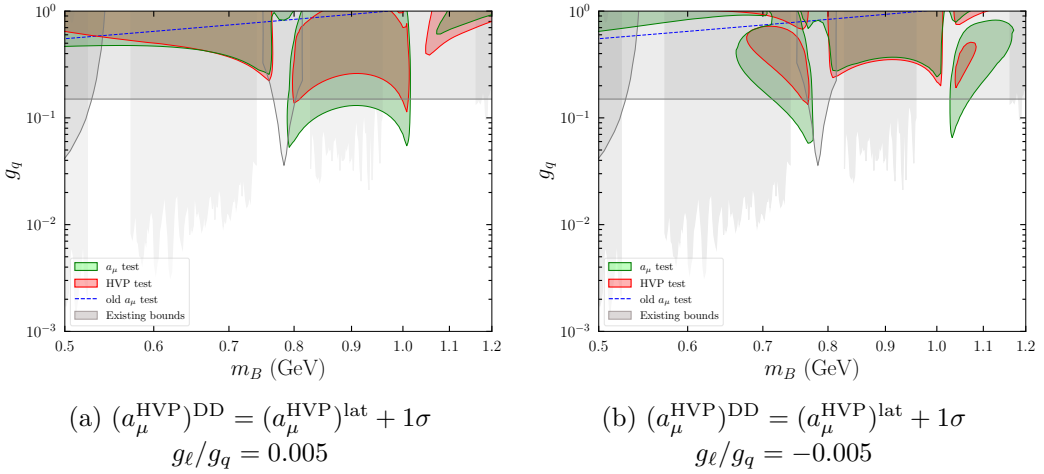


Figure 26: Parameter space of the quark coupling g_q as the function of the mass of B mass (m_B) for $g_\ell/g_q = 0.005$ (Fig. 26a) and $g_\ell/g_q = -0.005$ (Fig. 26b). We perform the lattice a_μ test (c.f. Eq. (2.14)) by taking the BMW result as the SM contribution. For the HVP test, we consider the possibility that $(a_\mu^{\text{HVP}})^{\text{DD}} = (a_\mu^{\text{HVP}})^{\text{lat}} + 1\sigma$. Rest matches Fig. 22.

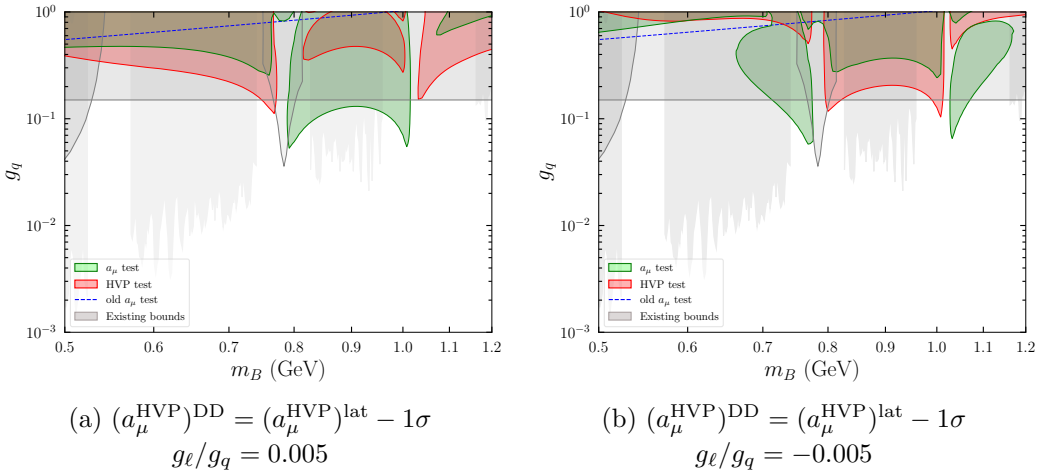


Figure 27: Parameter space of the quark coupling g_q as the function of the mass of B mass (m_B) for $g_\ell/g_q = 0.005$ (Fig. 27a) and $g_\ell/g_q = -0.005$ (Fig. 27b). We perform the lattice a_μ test (c.f. Eq. (2.14)) by taking the BMW result as the SM contribution. For the HVP test, we consider the possibility that $(a_\mu^{\text{HVP}})^{\text{DD}} = (a_\mu^{\text{HVP}})^{\text{lat}} - 1\sigma$. Rest matches Fig. 22.

C Window quantities

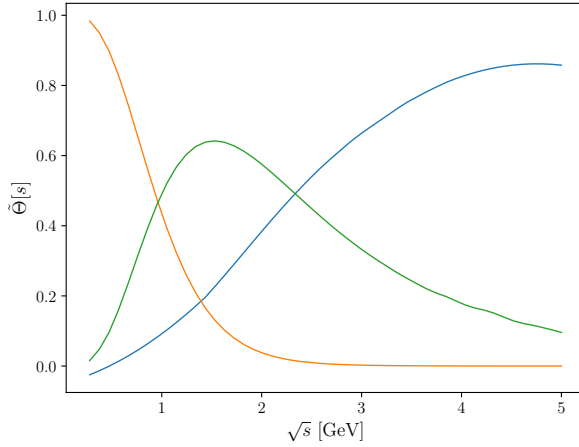


Figure 28: The weight functions of the various windows as a function of center-of-mass energy are shown; in blue (short-distance), green (intermediate-distance), and orange (long-distance).

	$a_\mu^{\text{SD}} \times 10^{10}$	$a_\mu^{\text{W}} \times 10^{10}$	$a_\mu^{\text{LD}} \times 10^{10}$
ETMC [13]	69.27(34)	235.0(1.1)	—
BMW 24 [20]	—	235.94(70)	—
CLS/Mainz [14–16]	68.85(45)	237.30(1.46)	423.2(5.4)
RBC/UKQCD [17, 18]	—	235.56(82)	411.4(4.9) (iso, LQC)
Fermilab/HPQCD/MILC [19]	69.01(21)	236.57(96)	—
Colangelo etc. '22 [69]	68.4(5)	229.4(1.4)	395.1(2.4)
Davier etc. '23 [26]	—	230.8(1.5) (BaBar) 227.3(1.3) (KLOE) 234.2(1.6) (CMD-3)	—
Benton '24 [80] (LQC)	46.96(48) (KNT19) 47.63(50) (CMD-3)	199.0(1.1) (KNT19) 205.8(1.6) (CMD-3)	389.9(1.7) (KNT19) 406.5(3.2) (CMD-3)

Table 1: Lattice (up) and data-driven (down) results of window observables.

In this section, we provide the data for the window quantities discussed in Section 5.2. The profile of the weight functions, $\tilde{\Theta}(s)$ as the function of the center of mass of energy s , is shown in Fig. 28 [69]. Many collaborations have calculated a_μ^{HVP} in the three windows, and we compile the results from some of them in Table 1. So far the intermediate distance window has the most results, while the results at the long-distance window appeared only very recently in [17] (iso-spin symmetric light-quark connected (lqc) contribution) and [16]. These results manifest good agreements with each other. Also shown in the table are recent results from the data-driven method [26, 69]. We also include the recent data-driven results

for the LQC-only contribution [80], to be compared with the results in [17]. We find that for the short-distance window, these two methods are consistent with each other. Large deviation shows up for the intermediate and long-distance regime when BaBar/KLOE results are used in the data-driven method, while results from CMD-3 agree with the lattice within the current error bars.

References

- [1] **Muon g-2** Collaboration, B. Abi et al., *Measurement of the Positive Muon Anomalous Magnetic Moment to 0.46 ppm*, *Phys. Rev. Lett.* **126** (2021), no. 14 141801, [[arXiv:2104.03281](https://arxiv.org/abs/2104.03281)].
- [2] **Muon g-2** Collaboration, D. P. Aguillard et al., *Measurement of the Positive Muon Anomalous Magnetic Moment to 0.20 ppm*, *Phys. Rev. Lett.* **131** (2023), no. 16 161802, [[arXiv:2308.06230](https://arxiv.org/abs/2308.06230)].
- [3] **Muon g-2** Collaboration, D. P. Aguillard et al., *Detailed report on the measurement of the positive muon anomalous magnetic moment to 0.20 ppm*, *Phys. Rev. D* **110** (2024), no. 3 032009, [[arXiv:2402.15410](https://arxiv.org/abs/2402.15410)].
- [4] **Muon g-2** Collaboration, G. W. Bennett et al., *Final Report of the Muon E821 Anomalous Magnetic Moment Measurement at BNL*, *Phys. Rev. D* **73** (2006) 072003, [[hep-ex/0602035](https://arxiv.org/abs/hep-ex/0602035)].
- [5] F. Jegerlehner, *The Anomalous Magnetic Moment of the Muon*, vol. 274. Springer, Cham, 2017.
- [6] **BaBar** Collaboration, B. Aubert et al., *Study of $e^+e^- \rightarrow \pi^+\pi^-\pi^0$ process using initial state radiation with BaBar*, *Phys. Rev. D* **70** (2004) 072004, [[hep-ex/0408078](https://arxiv.org/abs/hep-ex/0408078)].
- [7] M. N. Achasov et al., *Study of the process $e^+e^- \rightarrow \pi^+\pi^-\pi^0$ in the energy region \sqrt{s} from 0.98 GeV to 1.38 GeV*, *Phys. Rev. D* **66** (2002) 032001, [[hep-ex/0201040](https://arxiv.org/abs/hep-ex/0201040)].
- [8] M. N. Achasov et al., *Study of the process $e^+e^- \rightarrow \pi^+\pi^-\pi^0$ in the energy region \sqrt{s} below 0.98 GeV*, *Phys. Rev. D* **68** (2003) 052006, [[hep-ex/0305049](https://arxiv.org/abs/hep-ex/0305049)].
- [9] **KLOE-2** Collaboration, A. Anastasi et al., *Limit on the production of a new vector boson in $e^+e^- \rightarrow U\gamma$, $U \rightarrow \pi^+\pi^-$ with the KLOE experiment*, *Phys. Lett. B* **757** (2016) 356–361, [[arXiv:1603.06086](https://arxiv.org/abs/1603.06086)].
- [10] T. Aoyama et al., *The anomalous magnetic moment of the muon in the Standard Model*, *Phys. Rept.* **887** (2020) 1–166, [[arXiv:2006.04822](https://arxiv.org/abs/2006.04822)].
- [11] **CMD-3** Collaboration, F. V. Ignatov et al., *Measurement of the $e^+e^- \rightarrow \pi^+\pi^-$ cross section from threshold to 1.2 GeV with the CMD-3 detector*, *Phys. Rev. D* **109** (2024), no. 11 112002, [[arXiv:2302.08834](https://arxiv.org/abs/2302.08834)].
- [12] **CMD-3** Collaboration, F. V. Ignatov et al., *Measurement of the Pion Form Factor with CMD-3 Detector and its Implication to the Hadronic Contribution to Muon (g-2)*, *Phys. Rev. Lett.* **132** (2024), no. 23 231903, [[arXiv:2309.12910](https://arxiv.org/abs/2309.12910)].
- [13] C. Alexandrou et al., *Lattice calculation of the short and intermediate time-distance hadronic vacuum polarization contributions to the muon magnetic moment using twisted-mass fermions*, [arXiv:2206.15084](https://arxiv.org/abs/2206.15084).
- [14] M. Cè et al., *Window observable for the hadronic vacuum polarization contribution to the muon $g-2$ from lattice QCD*, [arXiv:2206.06582](https://arxiv.org/abs/2206.06582).

[15] S. Kuberski, M. Cè, G. von Hippel, H. B. Meyer, K. Ott nad, A. Risch, and H. Wittig, *Hadronic vacuum polarization in the muon $g - 2$: the short-distance contribution from lattice QCD*, *JHEP* **03** (2024) 172, [[arXiv:2401.11895](https://arxiv.org/abs/2401.11895)].

[16] D. Djukanovic, G. von Hippel, S. Kuberski, H. B. Meyer, N. Miller, K. Ott nad, J. Parrino, A. Risch, and H. Wittig, *The hadronic vacuum polarization contribution to the muon $g - 2$ at long distances*, [arXiv:2411.07969](https://arxiv.org/abs/2411.07969).

[17] **RBC, UKQCD** Collaboration, T. Blum et al., *The long-distance window of the hadronic vacuum polarization for the muon $g-2$* , [arXiv:2410.20590](https://arxiv.org/abs/2410.20590).

[18] **RBC, UKQCD** Collaboration, T. Blum et al., *Update of Euclidean windows of the hadronic vacuum polarization*, *Phys. Rev. D* **108** (2023), no. 5 054507, [[arXiv:2301.08696](https://arxiv.org/abs/2301.08696)].

[19] A. Bazavov et al., *Hadronic vacuum polarization for the muon $g - 2$ from lattice QCD: Complete short and intermediate windows*, [arXiv:2411.09656](https://arxiv.org/abs/2411.09656).

[20] A. Boccaletti et al., *High precision calculation of the hadronic vacuum polarisation contribution to the muon anomaly*, [arXiv:2407.10913](https://arxiv.org/abs/2407.10913).

[21] S. Borsanyi et al., *Leading hadronic contribution to the muon magnetic moment from lattice QCD*, *Nature* **593** (2021), no. 7857 51–55, [[arXiv:2002.12347](https://arxiv.org/abs/2002.12347)].

[22] L. Di Luzio, A. Masiero, P. Paradisi, and M. Passera, *New physics behind the new muon $g-2$ puzzle?*, *Phys. Lett. B* **829** (2022) 137037, [[arXiv:2112.08312](https://arxiv.org/abs/2112.08312)].

[23] L. Di Luzio, A. Keshavarzi, A. Masiero, and P. Paradisi, *Model Independent Tests of the Hadronic Vacuum Polarization Contribution to the Muon $g-2$* , [arXiv:2408.01123](https://arxiv.org/abs/2408.01123).

[24] C. Delaunay, B. Ohayon, and Y. Soreq, *Towards an Independent Determination of Muon $g-2$ from Muonium Spectroscopy*, *Phys. Rev. Lett.* **127** (2021), no. 25 251801, [[arXiv:2106.11998](https://arxiv.org/abs/2106.11998)].

[25] **BABAR, BaBar** Collaboration, J. P. Lees et al., *Study of the process $e^+e^- \rightarrow \pi^+\pi^-\pi^0$ using initial state radiation with BABAR*, *Phys. Rev. D* **104** (2021), no. 11 112003, [[arXiv:2110.00520](https://arxiv.org/abs/2110.00520)].

[26] M. Davier, A. Hoecker, A.-M. Lutz, B. Malaescu, and Z. Zhang, *Tensions in $e^+e^- \rightarrow \pi^+\pi^-(\gamma)$ measurements: the new landscape of data-driven hadronic vacuum polarization predictions for the muon $g - 2$* , *Eur. Phys. J. C* **84** (2024), no. 7 721, [[arXiv:2312.02053](https://arxiv.org/abs/2312.02053)].

[27] R. Balkin, C. Delaunay, M. Geller, E. Kajomovitz, G. Perez, Y. Shpilman, and Y. Soreq, *Custodial symmetry for muon $g-2$* , *Phys. Rev. D* **104** (2021), no. 5 053009, [[arXiv:2104.08289](https://arxiv.org/abs/2104.08289)].

[28] M. Passera, W. J. Marciano, and A. Sirlin, *The Muon $g-2$ and the bounds on the Higgs boson mass*, *Phys. Rev. D* **78** (2008) 013009, [[arXiv:0804.1142](https://arxiv.org/abs/0804.1142)].

[29] A. Keshavarzi, W. J. Marciano, M. Passera, and A. Sirlin, *Muon $g - 2$ and $\Delta\alpha$ connection*, *Phys. Rev. D* **102** (2020), no. 3 033002, [[arXiv:2006.12666](https://arxiv.org/abs/2006.12666)].

[30] N. M. Coyle and C. E. M. Wagner, *Resolving the muon $g - 2$ tension through Z' -induced modifications to σ_{had}* , *JHEP* **12** (2023) 071, [[arXiv:2305.02354](https://arxiv.org/abs/2305.02354)].

[31] L. B. Okun, *LIMITS OF ELECTRODYNAMICS: PARAPHOTONS?*, *Sov. Phys. JETP* **56** (1982) 502.

[32] B. Holdom, *Two $U(1)$'s and Epsilon Charge Shifts*, *Phys. Lett. B* **166** (1986) 196–198.

[33] P. Galison and A. Manohar, *TWO Z's OR NOT TWO Z's?*, *Phys. Lett. B* **136** (1984) 279–283.

[34] M. Pospelov, *Secluded U(1) below the weak scale*, *Phys. Rev. D* **80** (2009) 095002, [[arXiv:0811.1030](https://arxiv.org/abs/0811.1030)].

[35] N. Arkani-Hamed, D. P. Finkbeiner, T. R. Slatyer, and N. Weiner, *A Theory of Dark Matter*, *Phys. Rev. D* **79** (2009) 015014, [[arXiv:0810.0713](https://arxiv.org/abs/0810.0713)].

[36] J. D. Bjorken, R. Essig, P. Schuster, and N. Toro, *New Fixed-Target Experiments to Search for Dark Gauge Forces*, *Phys. Rev. D* **80** (2009) 075018, [[arXiv:0906.0580](https://arxiv.org/abs/0906.0580)].

[37] C. D. Carone and H. Murayama, *Possible light U(1) gauge boson coupled to baryon number*, *Phys. Rev. Lett.* **74** (1995) 3122–3125, [[hep-ph/9411256](https://arxiv.org/abs/hep-ph/9411256)].

[38] A. Aranda and C. D. Carone, *Limits on a light leptophobic gauge boson*, *Phys. Lett. B* **443** (1998) 352–358, [[hep-ph/9809522](https://arxiv.org/abs/hep-ph/9809522)].

[39] S. Tulin, *New weakly-coupled forces hidden in low-energy QCD*, *Phys. Rev. D* **89** (2014), no. 11 114008, [[arXiv:1404.4370](https://arxiv.org/abs/1404.4370)].

[40] **Belle-II** Collaboration, I. Adachi et al., *Measurement of the $e^+e^- \rightarrow \pi^+\pi^-\pi^0$ cross section in the energy range 0.62–3.50 GeV at Belle II*, [arXiv:2404.04915](https://arxiv.org/abs/2404.04915).

[41] M. E. Peskin and D. V. Schroeder, *An Introduction to quantum field theory*. Addison-Wesley, Reading, USA, 1995.

[42] P. Ilten, Y. Soreq, M. Williams, and W. Xue, *Serendipity in dark photon searches*, *JHEP* **06** (2018) 004, [[arXiv:1801.04847](https://arxiv.org/abs/1801.04847)].

[43] M. Endo, K. Hamaguchi, and G. Mishima, *Constraints on Hidden Photon Models from Electron g-2 and Hydrogen Spectroscopy*, *Phys. Rev. D* **86** (2012) 095029, [[arXiv:1209.2558](https://arxiv.org/abs/1209.2558)].

[44] **BaBar** Collaboration, J. P. Lees et al., *Search for a Dark Photon in e^+e^- Collisions at BaBar*, *Phys. Rev. Lett.* **113** (2014), no. 20 201801, [[arXiv:1406.2980](https://arxiv.org/abs/1406.2980)].

[45] **KLOE-2** Collaboration, D. Babusci et al., *Search for light vector boson production in $e^+e^- \rightarrow \mu^+\mu^-\gamma$ interactions with the KLOE experiment*, *Phys. Lett. B* **736** (2014) 459–464, [[arXiv:1404.7772](https://arxiv.org/abs/1404.7772)].

[46] **CMS** Collaboration, A. Hayrapetyan et al., *Search for direct production of GeV-scale resonances decaying to a pair of muons in proton-proton collisions at $\sqrt{s} = 13$ TeV*, *JHEP* **12** (2023) 070, [[arXiv:2309.16003](https://arxiv.org/abs/2309.16003)].

[47] P. Ilten, Y. Soreq, J. Thaler, M. Williams, and W. Xue, *Proposed Inclusive Dark Photon Search at LHCb*, *Phys. Rev. Lett.* **116** (2016), no. 25 251803, [[arXiv:1603.08926](https://arxiv.org/abs/1603.08926)].

[48] **LHCb** Collaboration, R. Aaij et al., *Search for Dark Photons Produced in 13 TeV pp Collisions*, *Phys. Rev. Lett.* **120** (2018), no. 6 061801, [[arXiv:1710.02867](https://arxiv.org/abs/1710.02867)].

[49] **LHCb** Collaboration, R. Aaij et al., *Search for $A' \rightarrow \mu^+\mu^-$ Decays*, *Phys. Rev. Lett.* **124** (2020), no. 4 041801, [[arXiv:1910.06926](https://arxiv.org/abs/1910.06926)].

[50] **Belle-II** Collaboration, M. Campajola, *Dark Sector first results at Belle II*, *Phys. Scripta* **96** (2021), no. 8 084005, [[arXiv:2208.01101](https://arxiv.org/abs/2208.01101)].

[51] **ARGUS** Collaboration, H. Albrecht et al., *An Upper Limit for Two Jet Production in Direct $\Upsilon(1s)$ Decays*, *Z. Phys. C* **31** (1986) 181.

[52] **ALEPH, DELPHI, L3, OPAL, LEP Electroweak** Collaboration, S. Schael et al., *Electroweak Measurements in Electron-Positron Collisions at W -Boson-Pair Energies at LEP*, *Phys. Rept.* **532** (2013) 119–244, [[arXiv:1302.3415](https://arxiv.org/abs/1302.3415)].

[53] **Particle Data Group** Collaboration, S. Navas et al., *Review of particle physics*, *Phys. Rev. D* **110** (2024), no. 3 030001.

[54] G. Gagliardi, R. Frezzotti, V. Lubicz, G. Martinelli, F. Sanfilippo, and S. Simula, *Lattice determination of the pion mass difference $M_{\pi^+} - M_{\pi^0}$ at order $\mathcal{O}(\alpha_{em})$ and $\mathcal{O}((m_d - m_u)^2)$ including disconnected diagrams.*, *PoS LATTICE2021* (2022) 255, [[arXiv:2112.01066](https://arxiv.org/abs/2112.01066)].

[55] M. Fabbrichesi, E. Gabrielli, and G. Lanfranchi, *The Dark Photon*, [arXiv:2005.01515](https://arxiv.org/abs/2005.01515).

[56] K. Agashe, A. Delgado, M. J. May, and R. Sundrum, *RS1, custodial isospin and precision tests*, *JHEP* **08** (2003) 050, [[hep-ph/0308036](https://arxiv.org/abs/hep-ph/0308036)].

[57] D. J. Gross and R. Jackiw, *Effect of anomalies on quasirenormalizable theories*, *Phys. Rev. D* **6** (1972) 477–493.

[58] J. A. Dror, R. Lasenby, and M. Pospelov, *New constraints on light vectors coupled to anomalous currents*, *Phys. Rev. Lett.* **119** (2017), no. 14 141803, [[arXiv:1705.06726](https://arxiv.org/abs/1705.06726)].

[59] J. A. Dror, R. Lasenby, and M. Pospelov, *Dark forces coupled to nonconserved currents*, *Phys. Rev. D* **96** (2017), no. 7 075036, [[arXiv:1707.01503](https://arxiv.org/abs/1707.01503)].

[60] L. Di Luzio, M. Nardecchia, and C. Toni, *Light vectors coupled to anomalous currents with harmless Wess-Zumino terms*, *Phys. Rev. D* **105** (2022), no. 11 115042, [[arXiv:2204.05945](https://arxiv.org/abs/2204.05945)].

[61] Q. Bonnifoy, L. Di Luzio, C. Grojean, A. Paul, and A. N. Rossia, *The anomalous case of axion EFTs and massive chiral gauge fields*, *JHEP* **07** (2021) 189, [[arXiv:2011.10025](https://arxiv.org/abs/2011.10025)].

[62] J. F. Kamenik, Y. Soreq, and J. Zupan, *Lepton flavor universality violation without new sources of quark flavor violation*, *Phys. Rev. D* **97** (2018), no. 3 035002, [[arXiv:1704.06005](https://arxiv.org/abs/1704.06005)].

[63] N. Bizot and M. Frigerio, *Fermionic extensions of the Standard Model in light of the Higgs couplings*, *JHEP* **01** (2016) 036, [[arXiv:1508.01645](https://arxiv.org/abs/1508.01645)].

[64] C. Fanelli and M. Williams, *Photoproduction of leptophobic bosons*, *J. Phys. G* **44** (2017), no. 1 014002, [[arXiv:1605.07161](https://arxiv.org/abs/1605.07161)].

[65] **KLOE-2** Collaboration, E. P. del Rio, *B boson search at KLOE/KLOE-2*, [arXiv:2112.10110](https://arxiv.org/abs/2112.10110).

[66] **Flavour Lattice Averaging Group (FLAG)** Collaboration, Y. Aoki et al., *FLAG Review 2024*, [arXiv:2411.04268](https://arxiv.org/abs/2411.04268).

[67] **RBC, UKQCD** Collaboration, T. Blum, P. A. Boyle, V. Gülpers, T. Izubuchi, L. Jin, C. Jung, A. Jüttner, C. Lehner, A. Portelli, and J. T. Tsang, *Calculation of the hadronic vacuum polarization contribution to the muon anomalous magnetic moment*, *Phys. Rev. Lett.* **121** (2018), no. 2 022003, [[arXiv:1801.07224](https://arxiv.org/abs/1801.07224)].

[68] D. Bernecker and H. B. Meyer, *Vector Correlators in Lattice QCD: Methods and applications*, *Eur. Phys. J. A* **47** (2011) 148, [[arXiv:1107.4388](https://arxiv.org/abs/1107.4388)].

[69] G. Colangelo, A. X. El-Khadra, M. Hoferichter, A. Keshavarzi, C. Lehner, P. Stoffer, and T. Teubner, *Data-driven evaluations of Euclidean windows to scrutinize hadronic vacuum polarization*, *Phys. Lett. B* **833** (2022) 137313, [[arXiv:2205.12963](https://arxiv.org/abs/2205.12963)].

[70] V. V. Bryzgalov and O. V. Zenin, *A comment on the impact of CMD-3 $e^+e^- \rightarrow \pi^+\pi^-$ cross section measurement on the SM $g_\mu - 2$ value*, [arXiv:2401.07204](https://arxiv.org/abs/2401.07204).

[71] **BaBar** Collaboration, J. P. Lees et al., *Precise Measurement of the $e^+e^- \rightarrow \pi^+\pi^-(\gamma)$ Cross Section with the Initial-State Radiation Method at BABAR*, *Phys. Rev. D* **86** (2012) 032013, [[arXiv:1205.2228](https://arxiv.org/abs/1205.2228)].

[72] **KLOE-2** Collaboration, A. Anastasi et al., *Combination of KLOE $\sigma(e^+e^- \rightarrow \pi^+\pi^-\gamma(\gamma))$ measurements and determination of $a_\mu^{\pi^+\pi^-}$ in the energy range $0.10 < s < 0.95$ GeV 2* , *JHEP* **03** (2018) 173, [[arXiv:1711.03085](https://arxiv.org/abs/1711.03085)].

[73] **KLOE** Collaboration, F. Ambrosino et al., *Measurement of $\sigma(e^+e^- \rightarrow \pi^+\pi^-)$ from threshold to 0.85 GeV 2 using Initial State Radiation with the KLOE detector*, *Phys. Lett. B* **700** (2011) 102–110, [[arXiv:1006.5313](https://arxiv.org/abs/1006.5313)].

[74] **KLOE** Collaboration, D. Babusci et al., *Precision measurement of $\sigma(e^+e^- \rightarrow \pi^+\pi^-\gamma)/\sigma(e^+e^- \rightarrow \mu^+\mu^-\gamma)$ and determination of the $\pi^+\pi^-$ contribution to the muon anomaly with the KLOE detector*, *Phys. Lett. B* **720** (2013) 336–343, [[arXiv:1212.4524](https://arxiv.org/abs/1212.4524)].

[75] M. N. Achasov et al., *Update of the $e^+e^- \rightarrow \pi^+\pi^-$ cross-section measured by SND detector in the energy region $400\text{-MeV} < s^{**}(1/2) < 1000\text{-MeV}$* , *J. Exp. Theor. Phys.* **103** (2006) 380–384, [[hep-ex/0605013](https://arxiv.org/abs/hep-ex/0605013)].

[76] **SND** Collaboration, M. N. Achasov et al., *Measurement of the $e^+e^- \rightarrow \pi^+\pi^-$ process cross section with the SND detector at the VEPP-2000 collider in the energy region $0.525 < \sqrt{s} < 0.883$ GeV*, *JHEP* **01** (2021) 113, [[arXiv:2004.00263](https://arxiv.org/abs/2004.00263)].

[77] **CMD-2** Collaboration, R. R. Akhmetshin et al., *High-statistics measurement of the pion form factor in the rho-meson energy range with the CMD-2 detector*, *Phys. Lett. B* **648** (2007) 28–38, [[hep-ex/0610021](https://arxiv.org/abs/hep-ex/0610021)].

[78] **CMD-2** Collaboration, V. M. Aul’chenko et al., *Measurement of the pion form-factor in the range 1.04-GeV to 1.38-GeV with the CMD-2 detector*, *JETP Lett.* **82** (2005) 743–747, [[hep-ex/0603021](https://arxiv.org/abs/hep-ex/0603021)].

[79] V. M. Aul’chenko et al., *Measurement of the $e^+e^- \rightarrow \pi^+\pi^-$ cross section with the CMD-2 detector in the 370 - 520-MeV c.m. energy range*, *JETP Lett.* **84** (2006) 413–417, [[hep-ex/0610016](https://arxiv.org/abs/hep-ex/0610016)].

[80] G. Benton, D. Boito, M. Golterman, A. Keshavarzi, K. Maltman, and S. Peris, *Data-driven results for light-quark connected and strange-plus-disconnected hadronic $g - 2$ short- and long-distance windows*, [arXiv:2411.06637](https://arxiv.org/abs/2411.06637).